

Date: October 30, 2018

1 **Prospects for GRB science with the *Fermi* Large Area Telescope**

2 D. L. Band^{1,2}, M. Axelsson³, L. Baldini⁴, G. Barbiellini^{5,6}, M. G. Baring⁷, D. Bastieri^{8,9},
3 M. Battelino¹⁰, R. Bellazzini⁴, E. Bissaldi¹¹, G. Bogaert¹², J. Bonnell², J. Chiang^{13,14},
4 J. Cohen-Tanugi¹⁵, V. Connaughton¹⁶, S. Cutini¹⁷, F. de Palma^{18,19}, B. L. Dingus²⁰,
5 E. do Couto e Silva¹³, G. Fishman²¹, A. Galli²², N. Gehrels^{2,23}, N. Giglietto^{18,19},
6 J. Granot²⁴, S. Guiriec^{15,16}, R. E. Hughes²⁵, T. Kamae¹³, N. Komin^{26,15}, F. Kuehn²⁵,
7 M. Kuss⁴, F. Longo^{5,6,14}, P. Lubrano²⁷, R. M. Kippen²⁰, M. N. Mazziotta¹⁹,
8 J. E. McEnery², S. McGlynn¹⁰, E. Moretti^{5,6}, T. Nakamori²⁸, J. P. Norris²⁹, M. Ohno³⁰,
9 M. Olivo⁵, N. Omodei^{4,14}, V. Pelassa¹⁵, F. Piron¹⁵, R. Preece¹⁶, M. Razzano⁴,
10 J. J. Russell¹³, F. Ryde¹⁰, P. M. Saz Parkinson³¹, J. D. Scargle³², C. Sgrò⁴,
11 T. Shimokawabe²⁸, P. D. Smith²⁵, G. Spandre⁴, P. Spinelli^{18,19}, M. Stamatikos²,
12 B. L. Winer²⁵, R. Yamazaki³³

¹Center for Research and Exploration in Space Science and Technology (CRESST), NASA Goddard Space Flight Center, Greenbelt, MD 20771

²NASA Goddard Space Flight Center, Greenbelt, MD 20771

³Stockholm Observatory, Albanova, SE-106 91 Stockholm, Sweden

⁴Istituto Nazionale di Fisica Nucleare, Sezione di Pisa, I-56127 Pisa, Italy

⁵Istituto Nazionale di Fisica Nucleare, Sezione di Trieste, I-34127 Trieste, Italy

⁶Dipartimento di Fisica, Università di Trieste, I-34127 Trieste, Italy

⁷Rice University, Department of Physics and Astronomy, MS-108, P. O. Box 1892, Houston, TX 77251, USA

⁸Istituto Nazionale di Fisica Nucleare, Sezione di Padova, I-35131 Padova, Italy

⁹Dipartimento di Fisica “G. Galilei”, Università di Padova, I-35131 Padova, Italy

¹⁰Department of Physics, Royal Institute of Technology (KTH), AlbaNova, SE-106 91 Stockholm, Sweden

¹¹Max-Planck Institut für extraterrestrische Physik, Giessenbachstraße, 85748 Garching, Germany

¹²Laboratoire Leprince-Ringuet, École polytechnique, CNRS/IN2P3, Palaiseau, France

¹³W. W. Hansen Experimental Physics Laboratory, Kavli Institute for Particle Astrophysics and Cosmology, Department of Physics and Stanford Linear Accelerator Center, Stanford University, Stanford, CA 94305

¹⁴Corresponding authors: J. Chiang, jchiang@slac.stanford.edu; F. Longo, francesco.longo@trieste.infn.it; N. Omodei, nicola.omodei@pi.infn.it.

¹⁵Laboratoire de Physique Théorique et Astroparticules, Université Montpellier 2, CNRS/IN2P3, Montpellier, France

¹⁶University of Alabama in Huntsville, Huntsville, AL 35899

¹⁷Agenzia Spaziale Italiana (ASI) Science Data Center, I-00044 Frascati (Roma), Italy

¹⁸Dipartimento di Fisica “M. Merlin” dell’Università e del Politecnico di Bari, I-70126 Bari, Italy

¹⁹Istituto Nazionale di Fisica Nucleare, Sezione di Bari, 70126 Bari, Italy

²⁰Los Alamos National Laboratory, Los Alamos, NM 87545, USA

²¹NASA Marshall Space Flight Center, Huntsville, AL 35805

²²INAF-Istituto di Astrofisica Spaziale e Fisica Cosmica, I-00133 Roma, Italy

²³University of Maryland, College Park, MD 20742

²⁴Centre for Astrophysics Research, University of Hertfordshire, College Lane, Hatfield AL10 9AB

²⁵Department of Physics, Center for Cosmology and Astro-Particle Physics, The Ohio State University, Columbus, OH 43210

13 **ABSTRACT**

14 The LAT instrument on the *Fermi* mission will reveal the rich spectral and
temporal gamma-ray burst phenomena in the >100 MeV band. The synergy
with *Fermi*'s GBM detectors will link these observations to those in the well-
explored 10–1000 keV range; the addition of the >100 MeV band observations
will resolve theoretical uncertainties about burst emission in both the prompt
and afterglow phases. Trigger algorithms will be applied to the LAT data both
onboard the spacecraft and on the ground. The sensitivity of these triggers will
differ because of the available computing resources onboard and on the ground.
Here we present the LAT's burst detection methodologies and the instrument's
GRB capabilities.

15 *Subject headings:* gamma rays: bursts

16 **1. Introduction**

17 The Large Area Telescope (LAT) on the *Fermi* Gamma-ray Space Telescope (formerly
18 GLAST—Gamma-ray Large Area Space Telescope) will turn the study of the 20 MeV to more
19 than 300 GeV spectral and temporal behavior of gamma-ray bursts (GRBs) from specula-
20 tion based on a few suggestive observations to a decisive diagnostic of the emission processes.
21 The burst observations of the Energetic Gamma-Ray Experiment Telescope (EGRET) on

²⁶Laboratoire AIM, CEA-IRFU/CNRS/Université Paris Diderot, Service d'Astrophysique, CEA Saclay, 91191 Gif sur Yvette, France

²⁷Istituto Nazionale di Fisica Nucleare, Sezione di Perugia, I-06123 Perugia, Italy

²⁸Department of Physics, Tokyo Institute of Technology, Meguro City, Tokyo 152-8551, Japan

²⁹Department of Physics and Astronomy, University of Denver, Denver, CO 80208

³⁰Institute of Space and Astronautical Science, JAXA, 3-1-1 Yoshinodai, Sagamihara, Kanagawa 229-8510, Japan

³¹Santa Cruz Institute for Particle Physics, Department of Physics and Department of Astronomy and Astrophysics, University of California at Santa Cruz, Santa Cruz, CA 95064

³²Space Sciences Division, NASA Ames Research Center, Moffett Field, CA 94035-1000

³³Department of Physical Science and Hiroshima Astrophysical Science Center, Hiroshima University, Higashi-Hiroshima 739-8526, Japan

22 the *Compton Gamma-Ray Observatory (CGRO)* suggested three types of high energy emis-
23 sion: an extrapolation of the 10–1000 keV spectral component to the >100 MeV band; an
24 additional spectral component during the <1 MeV ‘prompt’ emission; and high energy emis-
25 sion that lingers long after the prompt emission has faded away. The LAT’s observations,
26 in conjunction with the Gamma-ray Burst Monitor (GBM—8 keV to 30 MeV), will provide
27 unprecedented spectral-temporal coverage for a large number of bursts. The spectra from
28 these two instruments will cover seven and a half energy decades (<10 keV to >300 GeV;
29 see Fig. 1, which shows different theoretically-predicted spectra). Thus the LAT will explore
30 the rich phenomena suggested by the EGRET observations, probing the physical processes
31 in the extreme radiating regions.

32 In this paper we provide the scientific community interested in GRBs with an overview of
33 the LAT’s operations and capabilities in this research area. Our development of detection and
34 analysis tools has been guided by the previous observations and the theoretical expectations
35 for emission in the >100 MeV band (§ 2). The LAT is described in depth in an instrument
36 paper (Atwood et al. 2009), and therefore here we only provide a brief summary of the *Fermi*
37 mission and the LAT, focusing on issues relevant to burst detection and analysis (§ 3).
38 Simulations are the basis of our analysis of the mission’s burst sensitivity, and are largely
39 based on *CGRO* observations (§ 4). We use our simulation methodology to estimate the
40 ultimate burst sensitivity and the resulting burst flux distribution (§ 5). Both the LAT and
41 the GBM will apply burst detection algorithms onboard and on the ground, and the efficiency
42 of these methods will determine which bursts the LAT will detect, and with what latency
43 (§ 6). Once a burst has been detected, spectral and temporal analysis of LAT (and GBM)
44 data will be possible (§ 7). The burst observations by ground-based telescopes and other
45 space missions, particularly *Swift*, will complement the *Fermi* observations (§ 8). While
46 basic methods are in place for detecting and analyzing burst data, in-flight experience will
47 guide future work (§ 9).

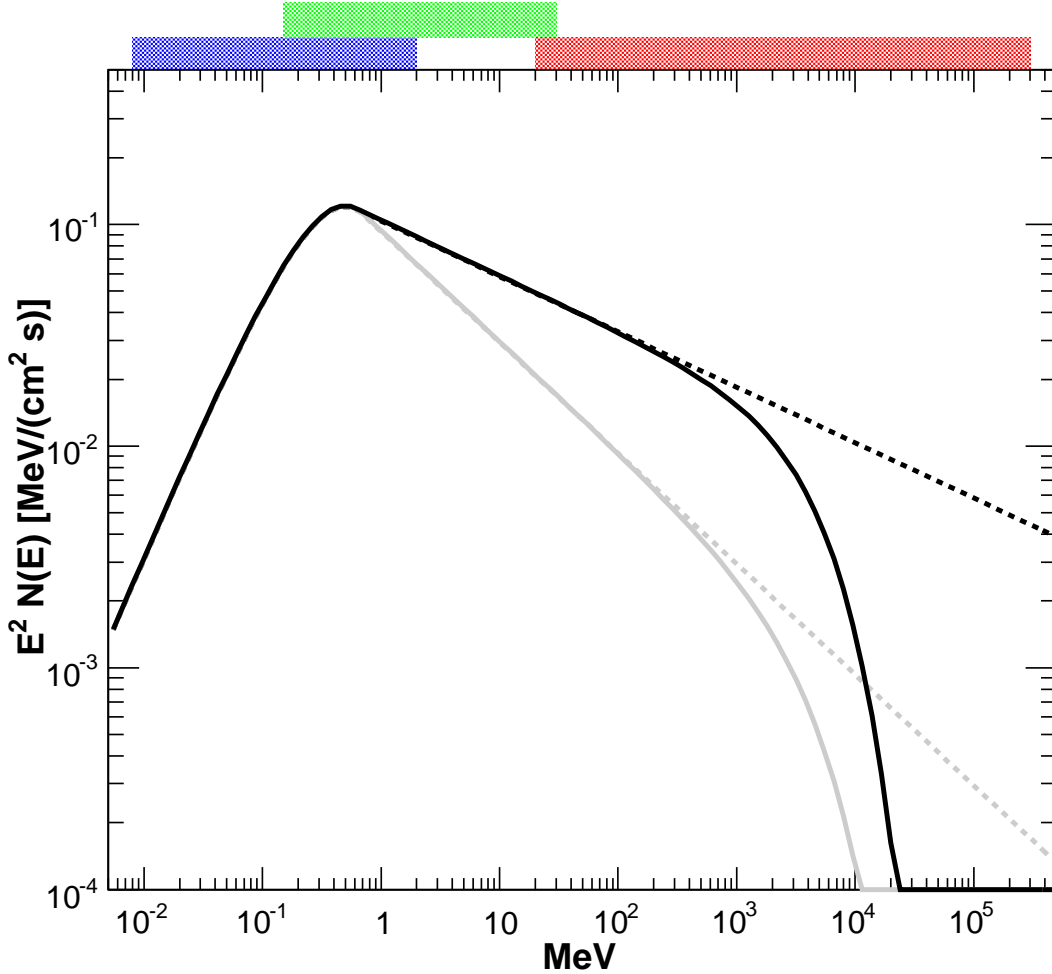


Fig. 1.— Simulated gamma-ray burst spectra, showing the broad energy range covered by *Fermi*: (from left to right) the GBM NaI (blue band: 8–2000 keV), the GBM BGO (green: 150 keV–30 MeV) and the LAT (red curve: 20 MeV to >300 GeV) detectors. The dashed curves are simple extrapolations of the typical GRB 10–1000 keV spectra into the GeV band, while the solid curves add an exponential cutoff that might result from absorption internal or external to the burst. The two different high energy photon indices $\beta=-2.25$ (black curves) and $\beta=-2.5$ (grey curves) demonstrate the dependence of the expected LAT flux on this photon index. There may be additional high energy components that are not known yet and are not shown in the figure.

2. Burst Physics Above 100 MeV

2.1. Previous Observations

The detectors of the *Compton Gamma-Ray Observatory (CGRO)* provided time-resolved spectra for a statistically well-defined burst population. These observations are the foundation of our expectations for *Fermi*'s discoveries, which have guided the development of analysis tools before launch.

The Burst And Transient Source Experiment (BATSE) on *CGRO* observed a large sample of bursts in the ~ 25 –2000 keV band with well-understood population statistics (Paciesas et al. 1999). Spectroscopy by the BATSE detectors found that the emission in this energy band could be described by the empirical four parameter ‘‘Band’’ function (Band et al. 1993)

$$N_{\text{Band}}(E|N_0, E_p, \alpha, \beta) = N_0 \begin{cases} E^\alpha \exp[-E(2 + \alpha)/E_p], & E \leq \frac{\alpha - \beta}{2 + \alpha} E_p \\ E^\beta \left[\frac{\alpha - \beta}{2 + \alpha} E_p \right]^{(\alpha - \beta)} \exp[\beta - \alpha], & E > \frac{\alpha - \beta}{2 + \alpha} E_p, \end{cases} \quad (1)$$

where α and β are the low and high energy photon indices, respectively, and E_p is the ‘peak energy’ which corresponds to the maximum of $E^2 N(E) \propto \nu f_\nu$ for the low energy component. Typically $\alpha \sim -0.5$ to -1 and β is less than -2 (Band et al. 1993; Preece et al. 2000; Kaneko et al. 2006); the total energy would be infinite if $\beta \geq -2$ unless the spectrum has a high energy cutoff. The observations of 37 bursts by the Compton Telescope (COMPTEL) on *CGRO* (0.75–30 MeV) are consistent with the BATSE observations of this spectral component (Hoover et al. 2005). Because of the relatively poor spectral resolution of the BATSE detectors (Briggs 1999), this functional form usually is a good description of spectra accumulated over both short time periods and entire bursts, even though bursts show strong spectral evolution (Ford et al. 1995). It is this 10–1000 keV ‘prompt’ component that is well-characterized and therefore provides a basis for quantitative predictions. A detailed duration-integrated spectral analysis (in 30 keV–200 MeV) of the prompt emission for 15 bright BATSE GRB performed by Kaneko et al. (2008) confirmed that only in few case there’s a significant high-energy excess with respect to low energy spectral extrapolations.

The burst observations by the Energetic Gamma-Ray Experiment Telescope (EGRET) on *CGRO* (20 MeV to 30 GeV) provide the best prediction of the LAT observations. EGRET observed different types of high energy burst phenomena. Four bursts had simultaneous emission in both the EGRET and BATSE energy bands, suggesting that the spectrum observed by BATSE extrapolates to the EGRET energy band (Dingus 2003). However, the correlation with the prompt phase pulses was hampered by the severe EGRET spark chamber

79 dead time (~ 100 ms/event) that was comparable or longer than the pulse timescales. The
 80 EGRET observations of these bursts suggest that the ~ 1 GeV emission often lasts longer
 81 than the lower energy emission, and thus results in part from a different physical origin. A
 82 similar behaviour is present also in GRB 080514B detected by AGILE (Giuliani et al. 2008).

83 Whether high energy emission is present in both long and short bursts is unknown. The
 84 four bursts with high energy emission detected by EGRET were all long bursts, although
 85 GRB 930131 is an interesting case. It was detected by BATSE (Kouveliotou et al. 1994) with
 86 duration of $T_{90}=14$ s¹ and found to have high-energy (>30 MeV) photons accompanying the
 87 prompt phase and possibly extending beyond (Sommer et al. 1994). The BATSE lightcurve
 88 is dominated by a hard initial emission lasting 1 sec and followed by a smooth extended
 89 emission. This burst may, therefore, have been one of those long bursts possibly associated
 90 with a merger and not a collapsar origin, commonly understood as the most probable origin
 91 for short and long burst respectively (Zhang 2007). Several events have now been identified
 92 that could fit into this category (Norris & Bonnell 2006) and their origin is still uncertain.
 93 LAT will make an important contribution in determining the nature of the high energy
 94 emission from similar events and a larger sample of bursts with detected high energy emission
 95 will determine whether the absence of high energy emission differentiates short from long
 96 bursts.

97 A high energy temporally resolved spectral component in addition to the Band function
 98 is clearly present in GRB 941017 (González et al. 2003); this component is harder than the
 99 low energy prompt component, and continues after the low energy component fades into the
 100 background. The time integrated spectra of both GRB 941017 and GRB 980923 show this
 101 additional spectral component (Kaneko et al. 2008).

102 Finally, the >1 GeV emission lingered for 90 minutes after the prompt low energy
 103 emission for GRB 940217, including an 18 GeV photon 1.5 hours after the burst trigger
 104 (Hurley et al. 1994). Whether this emission is physically associated with the lower energy
 105 afterglows is unknown.

106 These three empirical types of high energy emission—an extrapolation of the low energy
 107 spectra; an additional spectral component during the low energy prompt emission; and an
 108 afterglow—guide us in evaluating *Fermi*'s burst observation capabilities.

109 Because the prompt low energy component was characterized quantitatively by the
 110 BATSE observations while the EGRET observations merely demonstrated that different
 111 components were present, our simulations are based primarily on extrapolations of the

¹ T_{90} is the time over which 90% of the emission occurs in a specific energy band.

112 prompt low energy component from the BATSE band to the >100 MeV band. We rec-
 113 ognize that the LAT will probably detect additional spectral and temporal components, or
 114 spectral cutoffs, that are not treated in this extrapolation.

115 During the first few months of the *Fermi* mission, LAT detected already emission from
 116 three GRBs: 080825C (Bouvier et al. 2008), 080916C (Tajima et al. 2008) and 081024B
 117 (Omodei 2008). The rich phenomenology of high energy emission is confirmed in these
 118 three events, where spectral measurements over various order of magnitude were possible
 119 together with the detection of extended emission and spectral lags. In particular, the GRB
 120 080916C was bright enough to afford unprecedented broad-band spectral coverage in four
 121 distinct time intervals (Abdo et al. 2009), thereby offering new insights into the character of
 122 energetic bursts.

123 2.2. Theoretical Expectations

124 In the current standard scenario, the burst emission arises in a highly relativistic, un-
 125 steady outflow. Several different progenitor types could create this outflow, but the initial
 126 high optical depth within the outflow obscures the progenitor type. As this outflow gradu-
 127 ally becomes optically thin, dissipation processes within the outflow, as well as interactions
 128 with the surrounding medium, cause particles to be accelerated to high energies and loose
 129 some of their energy into radiation. Magnetic fields at the emission site can be strong and
 130 may be caused by a frozen-in component carried out by the outflow from the progenitor, or
 131 may be built up by turbulence or collisionless shocks. The emitted spectral distribution then
 132 depends on the details of the radiation mechanism, particle acceleration, and the dynamics
 133 of the explosion itself.

134 ‘Internal shocks’ result when a faster region catches up with a slower region within
 135 the outflow. ‘External shocks’ occur at the interface between the outflow and the ambient
 136 medium, and include a long-lived forward shock that is driven into the external medium
 137 and a short-lived reverse shock that decelerates the outflow. Thus the simple model of a
 138 one-dimensional relativistic outflow leads to a multiplicity of shock fronts, and many possible
 139 interacting emission regions.

140 As a result of the limited energy ranges of past and current experiments, most theories
 141 have not been clearly and unambiguously tested. *Fermi*’s GBM and LAT will provide
 142 an energy range broad enough to distinguish between different origins of the emission; in
 143 particular the unprecedented high-energy spectral coverage will constrain the total energy
 144 budget and radiative efficiency, as potentially most of the energy may be radiated in the LAT

145 range. The relations between the high and low energy spectral components can probe both
 146 the emission mechanism and the physical conditions in the emission region. The shape of
 147 the high energy spectral energy distribution will be crucial to discriminate between hadronic
 148 cascades and leptonic emission. The spectral breaks at high energy will constrain the Lorentz
 149 factor of the emitting region. Previously undetected emission components might be present
 150 in the light curves such as thermal emission. Finally, temporal analysis of the high energy
 151 delayed component will clarify the nature of the flares seen in the X-ray afterglows.

152 *2.2.1. Leptonic vs. Hadronic Emission Models*

153 It is very probable that particles are accelerated to very high energies close to the emis-
 154 sion site in GRBs. This could either be in shock fronts, where the Fermi mechanism or
 155 other plasma instabilities can act, or in magnetic reconnection sites. Two major classes of
 156 models—synchrotron and inverse Compton emission by relativistic electrons and protons,
 157 and hadronic cascades—have been proposed for the conversion of particle energy into ob-
 158 served photon radiation.

159 In the leptonic models, synchrotron emission by relativistic electrons can explain the
 160 10 keV–1 MeV spectrum in $\sim 2/3$ of bursts (e.g., see Preece et al. 1998), and inverse Compton
 161 (IC) scattering of low energy seed photons generally results in GeV band emission. These pro-
 162 cesses could operate in both internal and external shock regions (see, e.g., Zhang & Mészáros
 163 2001), with the relativistic electrons in one region scattering the ‘soft’ photons from another
 164 region (Fragile et al. 2004; Fan et al. 2005; Mészáros et al. 1994; Waxman 1997; Panaitescu et al.
 165 1998). Correlated high and low energy emission is expected if the same electrons radiate
 166 synchrotron photons and IC scatter soft photons. In Synchrotron Self-Compton (SSC) mod-
 167 els the electrons’ synchrotron photons are the soft photons and thus the high and low en-
 168 ergy components should have correlated variability (Guetta & Granot 2003; Galli & Guetta
 169 2008). However, SSC models tend to generate a broad νF_ν peak in the MeV band, and for
 170 bursts observed by *CGRO* this breadth has difficulty accommodating the observed spectra
 171 (Baring & Braby 2004). *Fermi*, with its broad spectral coverage enabled by the GBM and
 172 the LAT, is ideally suited for probing this issue further.

173 Alternatively, photospheric thermal emission might dominate the soft keV–MeV range
 174 during the early part of the prompt phase (Rees & Mészáros 2005; Ryde 2004, 2005). Such
 175 a component is expected when the outflow becomes optically thin, and would explain low
 176 energy spectra that are too hard for conventional synchrotron models (Crider et al. 1997;
 177 Preece et al. 1998, 2002). An additional power law component might underlie this thermal
 178 component and extend to high energy; this component might be synchrotron emission or

179 IC scattering of the thermal photons by relativistic electrons. Fits of the sum of thermal
 180 and power law models to BATSE spectra have been successful (Ryde 2004, 2005), but joint
 181 fits of spectra from the two types of GBM detectors and the LAT should resolve whether a
 182 thermal component is present (Battelino et al. 2007a,b).

183 In hadronic models relativistic protons scatter inelastically off the ~ 100 keV burst pho-
 184 tons ($p\gamma$ interactions) producing (among other possible products) high-energy, neutral pions
 185 (π^0) that decay, resulting in gamma rays and electrons that then radiate additional gamma
 186 rays. Similarly, if neutrons in the outflow decouple from protons, inelastic collisions between
 187 neutrons and protons can produce pions and subsequent high energy emission (Derishev et al.
 188 2000; Bahcall & Mészáros 2000). High energy neutrinos that may be observable are also
 189 emitted in these interactions (Waxman & Bahcall 1997). Many variants of hadronic cas-
 190 cade models have been proposed: high energy emission from proton-neutron inelastic col-
 191 lisions early in the evolution of the fireball (Bahcall & Mészáros 2000); proton-synchrotron
 192 and photo-meson cascade emission in internal shocks (e.g., Totani 1998; Zhang & Mészáros
 193 2001; Fragile et al. 2004; Gupta & Zhang 2007); and proton synchrotron emission in ex-
 194 ternal shocks (Bottcher & Dermer 1998). A hadronic model has been invoked to explain
 195 the additional spectral component observed in GRB 941017 (Dermer & Atoyan 2004). The
 196 emission in these models is predicted to peak in the MeV to GeV band (Bottcher & Dermer
 197 1998; Gupta & Zhang 2007), and thus would produce a clear signal in the LAT’s energy
 198 band. However, photon-meson interactions would result from a radiatively inefficient fireball
 199 (Gupta & Zhang 2007), which is in contrast with the high radiative efficiency that is sug-
 200 gested by *Swift* observations (Nousek et al. 2006; Granot et al. 2006). Thus, the hadronic
 201 mechanisms for gamma-ray production are many, but the *Fermi* measurements of the tem-
 202 poral evolution of the highest energy photons will provide strong constraints on these models,
 203 and moreover discern the existence or otherwise of distinct GeV-band components.

204 2.2.2. High-Energy Absorption

205 At high energies the outflow itself can become optically thick to photon-photon pair
 206 production, causing a break in the spectrum. Signatures of internal absorption will constrain
 207 the bulk Lorentz factor and adiabatic/radiative behavior of the GRB blast wave as a function
 208 of time (Baring & Harding 1997; Lithwick & Sari 2001; Guetta & Granot 2003; Baring 2006;
 209 Granot et al. 2008). Since the outflow might not be steady and may evolve during a burst,
 210 the breaks should be time-variable, a distinctive property of internal attenuation. Moreover,
 211 if the attenuated photons and their hard X-ray/soft gamma-ray target photons originate
 212 from proximate regions in the bursts, the turnovers will approximate broken power-laws.

213 Interestingly, the LAT has already provided palpable new advances in terms of constraining
 214 bulk motion in bursts. For GRB 080916C, the absence of observable attenuation turnovers
 215 up to around 13 GeV suggests that the bulk Lorentz factor may be well in excess of 500-800
 216 (Abdo et al. 2009).

217 Spectral cutoffs produced by internal absorption must be distinguished observationally
 218 from cutoffs caused by interactions with the extragalactic background. The optical depth
 219 of the Universe to high-energy gamma rays resulting from pair production on infrared and
 220 optical diffuse extragalactic background radiation can be considerable, thereby preventing
 221 the radiation from reaching us. These intervening background fields necessarily generate
 222 quasi-exponential turnovers familiar to TeV blazar studies, which may well be discernible
 223 from those resulting from internal absorption. Furthermore, their turnover energies should
 224 not vary with time throughout the burst, another distinction between the two origins for pair
 225 attenuation. In addition, the turnover energy for external absorption is expected above a few
 226 10’s of GeV while for internal absorption it may be as low as $\lesssim 1$ GeV (Granot et al. 2008).
 227 Although the external absorption may complicate the study of internal absorption, studies of
 228 the cutoff as a function of redshift can measure the universe’s optical energy emission out to
 229 the Population III epoch (with redshift > 7) (de Jager & Stecker 2002; Coppi & Aharonian
 230 1997; Kashlinsky 2005; Bromm & Loeb 2006).

231 *2.2.3. Delayed GeV Emission*

232 The observations of GRB 940217 (Hurley et al. 1994) demonstrated the existence of
 233 GeV-band emission long after the ~ 100 keV ‘prompt’ phase in at least some bursts. With
 234 the multiplicity of shock fronts and with synchrotron and IC components emitted at each
 235 front, many models for this lingering high energy emission are possible. In combination with
 236 the prompt emission observations and afterglow observations by *Swift* and ground-based
 237 telescopes, the LAT observations may detect spectral and temporal signatures to distinguish
 238 between the different models.

239 These models include: Synchrotron Self-Compton (SSC) emission in late internal shocks
 240 (LIS) (Zhang & Mészáros 2002; Wang et al. 2006; Fan et al. 2008; Galli & Guetta 2008);
 241 external IC (EIC) scattering of LIS photons by the forward shock electrons that radiate the
 242 afterglow (Wang et al. 2006); IC emission in the external reverse shock (RS) (Wang et al.
 243 2001; Granot & Guetta 2003; Kobayashi et al. 2007); and SSC emission in forward external
 244 shocks (Mészáros & Rees 1994; Dermer et al. 2000; Zhang & Mészáros 2001; Dermer 2007;
 245 Galli & Piro 2007).

246 A high energy IC component may be delayed and have broader time structures relative
 247 to lower energy components because the scattering may occur in a different region from
 248 where the soft photons are emitted (Wang et al. 2006). The correlation of GeV emission
 249 with X-ray afterglow flares observed by *Swift* would be a diagnostic for different models
 250 (Wang et al. 2006; Galli & Piro 2007; Galli & Guetta 2008).

251 2.3. Timing Analysis

252 The LAT’s low deadtime and large effective area will permit a detailed study of the
 253 high energy GRB light curve, which was impossible with the EGRET data as a result of the
 254 large deadtime that was comparable to typical widths of the peaks in the lightcurve. These
 255 measures are clearly important for determining the emission region size and the Lorentz
 256 factor in the emitting fireball.

257 The lightcurves of GRBs are frequently complex and diverse. Individual pulses display
 258 a hard-to-soft evolution, with E_p decreasing exponentially with the burst flux. One method
 259 of classifying bursts is to examine the spectral lag, which relates to the delay in the arrival of
 260 high energy and low energy photons (e.g., Norris et al. 2000; Foley et al. 2008). A positive
 261 lag value indicates hard-to-soft evolution (Kocevski & Liang 2003; Hafizi & Mochkovitch
 262 2007), i.e., high energy emission arrives earlier than low energy emission. This lag is a direct
 263 consequence of the spectral evolution of the burst as E_p decays with time. The distributions
 264 of spectral lags of short and long GRBs are noticeably different, with the lags of short GRBs
 265 concentrated in the range ± 30 ms (e.g., Norris & Bonnell 2006; Yi et al. 2006), while long
 266 GRBs have lags covering a wide range with a typical value of 100 ms (e.g., Hakkila et al.
 267 2007). Stamatikos et al. (2008b) study the spectral lags in the *Swift* data.

268 An anti-correlation has been discovered between the lag and the peak luminosity of
 269 the GRB at energies ~ 100 keV (Norris et al. 2000), using six BATSE bursts with definitive
 270 redshift. Brighter long GRBs tend to have a high peak luminosity and short lag, while weaker
 271 GRBs tend to have lower luminosities and longer lags. This “lag–luminosity relation” has
 272 been confirmed by using a number of *Swift* GRBs with known redshift (e.g., GRB 060218,
 273 with a lag greater than 100 s, Liang et al. 2006). *Fermi* will be able to determine if this
 274 relation extends to MeV-GeV energies.

275 A subpopulation of local, faint, long lag GRBs has been proposed by Norris (2002) from
 276 a study of BATSE bursts, which implies that events with low peak fluxes ($F_P(50–300 \text{ keV}) \sim$
 277 $0.25 \text{ ph cm}^{-2} \text{ s}^{-1}$) should be predominantly long lag GRBs. Norris (2002) successfully tested
 278 a prediction that these long lag events are relatively nearby and show some spatial anisotropy,

279 and found a concentration towards the local supergalactic plane. This has been confirmed
 280 with the GRBs observed by INTEGRAL (Foley et al. 2008) where it was found that $> 90\%$
 281 of the weak GRBs with a lag > 0.75 s were concentrated in the supergalactic plane².
 282 *Fermi* measures of long lag GRBs will confirm this hypothesis. An underluminous abun-
 283 dant population is inferred from observations of nearby bursts associated with supernovae
 284 (Soderberg et al. 2006).

285 Moreover, some Quantum Gravity (QG) theories predict an energy dependent speed-of-
 286 light (see e.g., Mattingly 2005), which is often parameterized as

$$v = c(1 - (E(z)/E_{qg})) \quad (2)$$

287 where $E(z)$ is the photon energy at a given redshift, $E(z) = E_{obs}(1 + z)$, and E_{qg} is the QG
 288 scale, which may be of order $\sim 10^{19}$ GeV. This energy-dependence can be measured from
 289 the difference in the arrival times of different-energy photons that were emitted at the same
 290 time; measurements thus far give E_{qg} greater than a few times 10^{17} GeV. Such photons might
 291 be emitted in sharp burst pulses (Amelino-Camelia et al. 1998); measurements have been
 292 attempted (Schaefer 1999; Boggs et al. 2004). The most difficult roadblock to reliable quan-
 293 tum gravity detections or upper limits results from the difficulty in discriminating against
 294 time delays inherent in the emission at the site of the GRB itself, and known to exist from
 295 previous observations. This problem can be addressed by studying a sample of bursts at
 296 different redshifts, or otherwise calibrating this effect.

297 With the energy difference between the GBM’s low energy end and the LAT’s high
 298 energy end, the good event timing by both the GBM and the LAT, and the LAT’s sensitivity
 299 to high energy photons, the *Fermi* mission will place interesting limits on E_{qg} .

²A possible counterargument has been recently claimed by Xiao & Schaefer (2009)

3. Description of the *Fermi* Mission

3.1. Mission Overview

Fermi was launched on June 11, 2008, into a 96.5 min circular orbit 565 km above the Earth with an inclination of 25.6° to the Earth’s equator. During the South Atlantic Anomaly passages (approximately 17% of the time, on average) the *Fermi* detectors do not take scientific data. In *Fermi*’s default observing mode the LAT’s pointing is offset 35° from the zenith direction perpendicular to the orbital plane; the pointing will be rocked from one side of the orbital plane to the other once per orbit. This observing pattern results in fairly uniform LAT sky exposure over two orbits; the uniformity is increased by the 54 d precession of the orbital plane.

The mission’s telemetry is downlinked 6–8 times per day on the Ku band through the Tracking and Data Relay Satellite System (TDRSS).³ The time between these downlinks, the transmission time through TDRSS and the processing at the LAT Instrument Science and Operations Center (LISOC) result in a latency of 6 hours between an observation and the availability of the resulting LAT data for astrophysical analysis. In addition, when burst detection software for either detector triggers, messages are sent to the ground through TDRSS with a ~ 15 s latency. The mission’s burst operations are described in greater detail below.

3.2. The Large Area Telescope (LAT)

A product of an international collaboration between NASA, DOE and many scientific institutions across France, Italy, Japan and Sweden, the LAT is a pair conversion telescope designed to cover the energy band from 20 MeV to greater than 300 GeV. The LAT is described in greater depth in Atwood et al. (2009) and here we summarize salient features useful for understanding the detector’s burst capabilities. The LAT consists of an array of 4×4 modules, each including a tracker-converter based on Silicon Strip Detector (SSD) technology and a 8.5 radiation lengths CsI hodoscopic calorimeter. High energy incoming gamma-rays convert into electron-positron pairs in one of the tungsten layers that are interleaved with the SSD planes; the pairs are then tracked to point back to the original photons’ direction and their energy is measured by the calorimeter. A segmented anti-coincident shield surrounding the whole detector ensures the necessary background rejection power

³See <http://msl.jpl.nasa.gov/Programs/tdrss.html>

330 against charged particles, whose flux outnumbers that of gamma-rays by several orders of
 331 magnitude, and reduce the data volume to fit in the telemetry bandwidth.

332 Key points of the LAT design are: wide Field-Of-View (FOV—more than 2 sr), large
 333 effective area and excellent Point Spread Function (PSF—see Fig. 2), short dead time (~ 25
 334 μs per event) and good energy resolution (of the order of 10% in the central region of the
 335 active energy range). As a result, the LAT is the most sensitive high energy gamma-ray
 336 detector ever flown. The study of gamma-ray bursts (GRBs) will take particular advantage
 337 of the improvement in angular resolution—we estimate that two or three photons above 1
 338 GeV will localize a bursts to ~ 5 arcminutes. The reduced dead time will allow the study
 339 of the sub-structure of the GRB pulses, typically of the order of milliseconds (Walker et al.
 340 2000), with a time resolution that has never before been accessible at GeV energies.

341 The data telemetered to the ground consists of the signals from different parts of the
 342 LAT; from these signals the ground software must ‘reconstruct’ the events and filter out
 343 events that are unlikely to be gamma-rays. Therefore, the Instrument Response Functions
 344 (IRFs) depend not only on the hardware but also on the reconstruction and event selection
 345 software. For the same set of reconstructed events trade-offs in the event selection between
 346 retaining gamma rays and rejecting background result in different event classes. There are
 347 currently three standard event classes—the *transient*, *source* and *diffuse* event classes—that
 348 are appropriate for different scientific analyses (as their names suggest). Less severe cuts
 349 increase the photon signal (and hence the effective area) at the expense of an increase in the
 350 non-photon background and a degradation of the PSF and the energy resolution.

351 The least restrictive class, the transient event class, is designed for bright, transitory
 352 sources that are not background-limited. We expect that the on-ground event rate over the
 353 whole FOV above 100 MeV will be 2 Hz for the transient class and 0.4 Hz for the source
 354 class. In both cases we expect about one non-burst event per minute within the area of the
 355 PSF around the burst position. Consequently, there should be essentially no background
 356 during the prompt emission (with a typical duration of less than a minute) so that the
 357 transient class is the most appropriate—and in fact is the one used for producing all the
 358 results presented in this paper. On the other hand, the analysis of afterglows, which may
 359 linger for a few hours, will need to account for the non-burst background, at least in the low
 360 region of the energy spectrum, where the PSF is larger (see Fig. 2).

361 The onboard flight software also performs event reconstructions for the burst trigger.
 362 Because of the available computer resources, the onboard event selection is not as discrim-
 363 inating as the on-ground event selection, and therefore the onboard burst trigger is not as
 364 sensitive because the astrophysical photons are diluted by a larger background flux. Simi-
 365 larly, larger localization uncertainties result from the larger onboard PSF, as shown by the

366 left-hand panel of Fig. 2.

367 **3.3. *Fermi* Gamma-ray Burst Monitor (GBM)**

368 The GBM detects and localizes bursts, and extends *Fermi*'s burst spectral sensitivity
369 to the energy range between 8 keV and 30 MeV or more. It consists of 12 NaI(Tl) (8–
370 1000 keV) and 2 BGO (0.15–> 30 MeV) crystals read by photomultipliers, arrayed with
371 different orientations around the spacecraft. The GBM monitors more than 8 sr of the sky,
372 including the LAT's FOV, and localizes bursts with an accuracy of $< 15^\circ$ (1σ) onboard,
373 ($< 3^\circ$ on ground), by comparing the rates in different detectors. The GBM is described in
374 greater detail in Meegan et al. (2009, submitted).

375 **3.4. *Fermi*'s Burst Operations**

376 Both the GBM and the LAT have burst triggers. When either instrument triggers, a no-
377 tice is sent to the ground through the TDRSS within ~ 15 s after the burst was detected and
378 then disseminated by the Gamma-ray burst Coordinates Network (GCN)⁴ to observatories
379 around the world. This initial notice is followed by messages with localizations calculated
380 by the flight software of each detector. Additional data (e.g., burst and background rates)
381 are also sent down by the GBM through TDRSS for an improved rapid localization on the
382 ground by a dedicated processor.

383 Updated positions are calculated from the full datasets from each detector that are
384 downlinked with a latency of a few hours. Scientists from both instrument teams analyze
385 these data, and if warranted by the results, confer. Conclusions from these analyses are
386 disseminated through GCN Circulars, free-format text that is e-mailed to scientists who
387 have subscribed to this service. Both Notices and Circulars are posted on the GCN website.

388 If the observed burst fluxes in either detector exceed pre-set thresholds (which are higher
389 for bursts detected by the GBM outside the LAT's FOV), the FSW sends a request that the
390 spacecraft slew to point the LAT at the burst location for a followup pointed observation;
391 currently a 5 hr observation is planned.

392 In addition to the search for GRB onboard the LAT and manual follow-up analysis by
393 duty scientists, there is also automated processing of the full science data. This processing

⁴See <http://gcn.gsfc.nasa.gov/>

³⁹⁴ performs an independent search for transient events in the LAT data, to greater sensitivity
³⁹⁵ than is possible onboard, and also performs a counterpart search for all GRB detected within
³⁹⁶ the LAT FoV. This is described in greater detail in § 6.3.

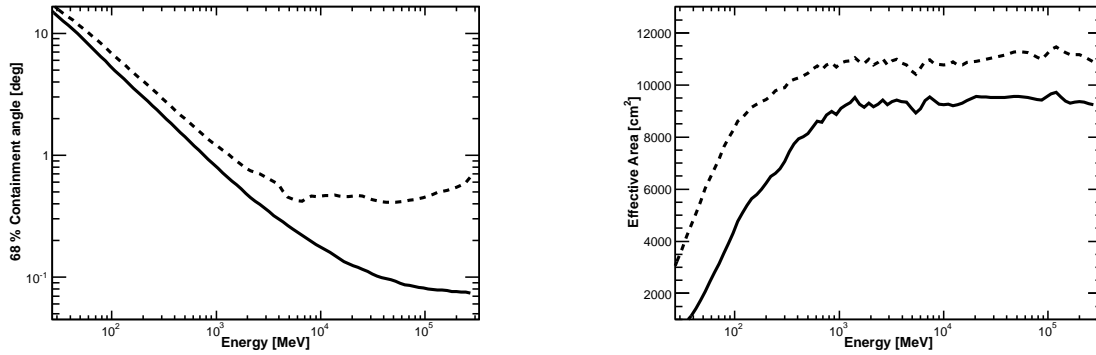


Fig. 2.— **Left**: Comparison of the estimated Point Spread Function (PSF) for the onboard and on-ground event reconstruction and selection. The black solid curve is the 68% containment angle on-axis for the transient event class, while the dashed curve represents the performance of the onboard reconstruction. **Right**: Comparison of the estimated onboard (dashed) and on-ground (solid black curve) on-axis effective areas. These estimates of the instrument response are based on simulations of the LAT.

4. Burst Simulations

397

398 We test the *Fermi* burst detection and analysis software with simulated data. These
 399 simulated data are based on our expectations for burst emission in the LAT and GBM
 400 spectral bands (see § 2), and on models of the instrument response of these two detectors.
 401 Since bursts undoubtedly differ from our theoretical expectations, our calculations are more
 402 reliable in showing the mission’s sensitivity to specific bursts than in estimating the number
 403 of bursts that will be detected.

404 We have two ‘GRB simulators’ that model the burst flux incident on each detector
 405 (Battelino et al. 2007a). The primary is the phenomenological simulator—described in
 406 greater detail below in § 4.1—that draws burst parameters from observed distributions. We
 407 have also created a physical simulator (Omodei 2005; Omodei & Norris 2007; Omodei et al.
 408 2007) that calculates the synchrotron emission from the collision of shells in a relativistic
 409 outflow (the internal shock model—Piran 1999). For a given analysis we assemble an ensem-
 410 ble of simulated bursts using one of these GRB simulators. To simulate a LAT observation
 411 of each burst in this ensemble we create a realization of the photon flux, resulting in a
 412 list of simulated photons incident on the LAT. The LAT’s response to this photon flux is
 413 processed in one of two software paths. The first uses ‘GLEAM’, which performs a Monte
 414 Carlo simulation of the propagation of the photon and its resulting particle shower in the
 415 LAT (using the GEANT4 toolkit (Agostinelli et al. 2003)) and the detection of particles in
 416 the different LAT components (Atwood et al. 2004; Baldini et al. 2006). The photon is then
 417 ‘reconstructed’ from this simulated instrument response by the same software that processes
 418 real data. Thus GLEAM maps the incident photons into observed events. Our second, faster,
 419 processing pathway uses the instrument response functions to map the photons into events
 420 directly. We note that both approaches use the same input—a list of incident photons—and
 421 result in the same output—a list of ‘observed’ events in one of the event classes. In both
 422 approaches GRBs can be combined with other source types (such as stationary and flar-
 423 ing AGN, solar flares, supernova remnants, pulsars) to build a very complex model of the
 424 gamma-ray sky.

425 The GRB simulators also provide the input to the GBM simulation software. In this case
 426 the GRB simulators produce a time series of spectral parameters (usually the parameters for
 427 the ‘Band’ function—Band 2003—discussed above in § 2.1). The GBM simulation software
 428 samples the burst spectrum to create a list of incident photons and then uses a model of
 429 the GBM response to determine whether each photon is ‘detected,’ and if so, in which
 430 energy channel (simulating the GBM’s finite spectral resolution). Based on a model from
 431 the BATSE observations, background counts are added to the burst counts. The GBM
 432 simulation software outputs count lists, response matrices and background spectra in the

433 standard FITS formats used by software such as XSPEC.⁵

434 Because the GRB simulators provide input to both LAT and GBM simulations, sim-
 435 ulated LAT and GBM data can be produced for the same bursts, allowing joint analyses.
 436 The *Fermi* mission developed the ‘Standard Analysis Environment’ (SAE) to analyze both
 437 LAT and GBM data. Data can be binned in time, resulting in light curves (see, for example,
 438 Fig. 3), or in spectra that can be analyzed using a tool such as XSPEC. As will be described
 439 in § 7, joint fits of GBM and LAT data may cover an energy band larger than seven orders of
 440 magnitude (see Fig. 1). Consequently, *Fermi* will be a very powerful tool for understanding
 441 the correlation between low-energy and high-energy GRB spectra.

442 4.1. Phenomenological Burst Model

443 The phenomenological GRB simulator that is used for most of our simulations draws
 444 from observed spectral and temporal distributions to construct model gamma-ray bursts.
 445 This modeling assumes that bursts consist of a series of pulses that can be described by a
 446 universal family of functions (Norris et al. 1996)

$$I(t) = A \begin{cases} \exp[-(|t - t_0|/\sigma_r)^\nu], & t \leq t_0 \\ \exp[-(|t - t_0|/\sigma_d)^\nu], & t > t_0 \end{cases} \quad (3)$$

447 where σ_r and σ_d parameterize the rise and decay timescale, and ν provides the ‘peakiness’ of
 448 the pulse. Although empirically $\sigma_r \sim 0.33 \sigma_d^{0.86}$, we approximate this relation as $\sigma_r \sim \sigma_d/3$.
 449 The pulse Full Width at Half Maximum (FWHM) is

$$W = (\sigma_r + \sigma_d) \ln(2)^{1/\nu}. \quad (4)$$

450 Pulses are observed to narrow at higher energy in the BATSE energy band (Davis et al.
 451 1994; Norris et al. 1996; Fenimore et al. 1995). Although the statistics in the EGRET data
 452 were insufficient to determine whether this narrowing continues in the >100 MeV band,
 453 our phenomenological model assumes that it does. We assume that the FWHM energy
 454 dependence is $W(E) \propto E^{-\xi}$ where ξ is ~ 0.4 (Fenimore et al. 1995; Norris et al. 1996). Thus,
 455 we give the pulse shape in eq. 3 an energy dependence by setting

$$\begin{cases} \sigma_d(E) = 0.75 \times \ln(2)^{-1/\nu} W_0 (E/20 \text{ keV})^{-\xi} \\ \sigma_r(E) = 0.25 \times \ln(2)^{-1/\nu} W_0 (E/20 \text{ keV})^{-\xi} \end{cases}, \quad (5)$$

⁵See <http://heasarc.nasa.gov/xanadu/xspec/>

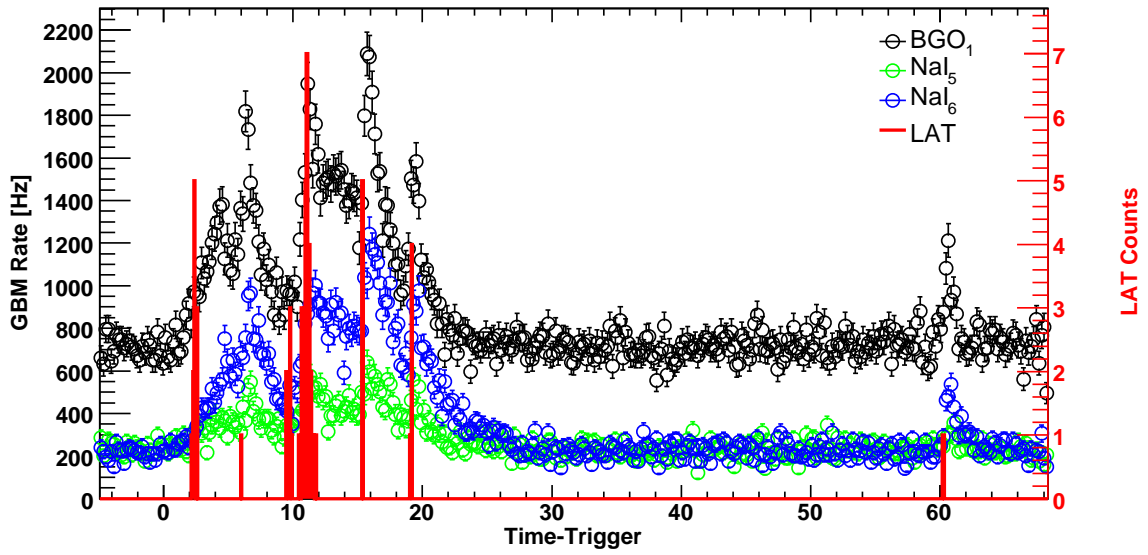


Fig. 3.— Simulated count rate light curve for a BGO detector, two NaI detectors, and the LAT for one simulated burst. In this model of the burst spectral evolution, the LAT detects counts at the beginning of each pulse; the correlation of the LAT and GBM light curves will be a powerful diagnostic of the emission processes. The simulation predicts that the LAT would detect a total of 42 gamma rays above 30 MeV in this moderately bright burst of 1 s peak flux of $63.37 \text{ ph cm}^{-2} \text{ s}^{-1}$ between 30 and 500 keV.

456 where W_0 is the FWHM at 20 keV. Burst spectra in the 10–1000 keV band are well-described
 457 by the ‘Band’ function (Band et al. 1993) parameterized in eq. 1. Empirically the Band
 458 function is an adequate description of burst spectra accumulated on short timescales (e.g.,
 459 shorter than a pulse width) and over an entire burst. This may be due in part to the poor
 460 spectral resolution of scintillation detectors (such as BATSE and the GBM), but we will treat
 461 this as a physical characteristic of gamma-ray bursts. In the resulting model, the flux $f(t, E)$
 462 is a product of a Band function with spectral indices α' and β' and the energy-dependent
 463 pulse shape $I(t, E)$ (eq. 3 with eq. 5)

$$f(t, E) = I(t, E) N_{\text{Band}}(E|N_0, E_p, \alpha', \beta') \quad \text{ph cm}^{-2} \text{ s}^{-1} \text{ keV}^{-1}. \quad (6)$$

464 Note that this spectrum is not strictly a Band function because the pulse shape function
 465 does not have a power law energy dependence.

466 The spectrum integrated over the entire burst is a Band function that is proportional to
 467 the product $W(E)N_{\text{Band}}(E|N_0, E_p, \alpha', \beta')$. Because $W(E)$ is a power law with spectral index
 468 $-\xi$, the spectral indices α and β for the integrated spectrum are different from the indices for
 469 the instantaneous flux (eq. 6)

$$\begin{aligned} \int_{-\infty}^{\infty} f(t, E) dt &= N_{\text{Band}}(E|N_0, E_p, \alpha, \beta)T = A_0 N_{\text{Band}}(E|N_0, E_p, \alpha', \beta') W(E) \\ &= A_0 W_0 N_{\text{Band}}(E|N_0, E_p, \alpha' - \xi, \beta' - \xi) \end{aligned} \quad (7)$$

470 where T is the burst duration and all the normalizing factors resulting from the integration
 471 are incorporated in A_0 . Thus the flux for a single GRB is the sum of many pulses of the
 472 form

$$f(t, E) = I(t, E)N_{\text{Band}}(E|N_0, E_p, \alpha + \xi, \beta + \xi). \quad (8)$$

473 Drawn from observed burst distributions, the same spectral parameters E_p , α and β are used
 474 for a given simulated burst. The number of pulses and parameters of each pulse (amplitude,
 475 width and peakedness) are also sampled from observed distributions (Norris et al. 1996).

476 Alternative spectral models have also been simulated; for example, Battelino et al.
 477 (2007a) describe simulations with a strong thermal photospheric component.

478 **5. Semi-Analytical Sensitivity Estimates**

479 The design of the LAT detector provides an ultimate burst sensitivity, regardless of
 480 whether the detection and analysis software achieves this ultimate limit. Thus in this section
 481 we estimate the LAT’s burst detection and localization capabilities, and the expected flux
 482 distribution. The following section describes the current burst detection algorithms.

483 **5.1. Semi-Analytical Estimation of the Burst Detection Sensitivity**

484 In this subsection we compute the LAT’s burst detection sensitivity using a semi-
 485 analytical approach based on the likelihood ratio test introduced by Neyman & Pearson
 486 (1928). This test is applied extensively to photon-counting experiments (Cash 1979) and
 487 has been used to analyze the gamma-ray data from COS-B (Pollock et al. 1981, 1985) and
 488 EGRET (Mattox et al. 1996). The statistic for this test is the likelihood for the null hypoth-
 489 esis for the data divided by the likelihood for the alternative hypothesis, here that burst flux
 490 is present. This methodology is the basis of the likelihood tool that will be used to analyze
 491 LAT observations; here we perform a semi-analytic calculation for the simple case of a point
 492 source on a uniform background.

493 In photon-counting experiments, the natural logarithm of the likelihood for a given
 494 model can be written as

$$\ln(L) = \sum_{photons} \ln(M_i) - N_{pred} + \text{constant} \quad (9)$$

495 where M_i is the predicted photon density at the position and time of i th observed count,
 496 and N_{pred} is the predicted total number of counts. We compare the log likelihood for the null
 497 hypothesis that only background counts are present versus the hypothesis that both burst
 498 and background counts are present.

499 The expected number of counts from a burst flux $S(E)$ is

$$N_S = T_{obs} \int_{\Delta\Omega} \int_{E_1}^{E_2} A_{eff}(E) S(E) F(E, \Omega) dE d\Omega \quad (10)$$

500 while the expected number of counts from a background flux $B(E)$ (assumed to be uniformly
 501 distributed over the sky) is

$$N_B = T_{obs} \int_{E_1}^{E_2} A_{eff}(E) B(E) dE \Delta\Omega \quad (11)$$

502 where A_{eff} is the effective area and $F(E, \Omega)$ is the normalized PSF (which therefore does
 503 not show up in eq. 11). Note that $B(E)$ varies significantly over the sky, but our assumption
 504 is that it is constant over $\Delta\Omega$.

505 The logarithm of the likelihood of the null hypothesis is

$$\ln(L_0) = T_{obs} \int_{\Delta\Omega} \int_{E_1}^{E_2} A_{eff}(E) [S(E)F(E, \Omega) + B(E)] \times \ln(A_{eff}(E)B(E)) dE d\Omega - N_B \quad . \quad (12)$$

506 The actual count rate is assumed to result from both background and burst flux while the
 507 predicted count rates (the M_i in eq. 9 and the total number of counts N_{pred}) are calculated
 508 only for the background flux (the null hypothesis).

509 Similarly, the logarithm of the likelihood of the hypothesis that a burst is present is

$$\ln(L_1) = \left[T_{obs} \int_{\Delta\Omega} \int_{E_1}^{E_2} A_{eff}(E) [S(E)F(E, \Omega) + B(E)] \times \ln(A_{eff}(E) [S(E)F(E, \Omega) + B(E)]) dE d\Omega \right] - (N_S + N_B) \quad . \quad (13)$$

510 Here both the actual and predicted count rates are calculated for both burst and background
 511 fluxes.

512 Wilks' theorem (Wilks 1938) defines the Test Statistic as $T_S = -2(\ln(L_0) - \ln(L_1))$, and
 513 states that T_S is distributed (asymptotically) as a χ^2 distribution of m degrees of freedom,
 514 where m is the number of burst parameters. From eqs. 12 and 13 T_S is

$$T_S = 2 T_{obs} \int_{\Delta\Omega} \int_{E_1}^{E_2} A_{eff}(E) B(E) [(1 + G(E, \Omega)) \ln(1 + G(E, \Omega)) - G(E, \Omega)] dE d\Omega \quad (14)$$

515 where we have defined a signal-to-noise ratio $G(E, \Omega) = S(E)F(E, \Omega)/B(E)$.

516 The significance of a source detection in standard deviation units is calculated as $N_\sigma =$
 517 $\sqrt{T_S}$ in the case $m = 1$ (χ^2 with 1 dof). Here we assume that Wilks' theorem holds, which
 518 might be not absolutely true in a low-count regime (see, in particular, the discussion in
 519 § 6.5). However, we will see that this method gives a robust estimate of the LAT sensitivity
 520 to GRBs. We can use this method to estimate the LAT sensitivity to GRB.

521 In our modeling we assume the burst has a 'Band' function spectrum (see eq. 1) and that
 522 the flux is constant over a duration T_{GRB} . Since we seek the optimal detection sensitivity,
 523 we calculate T_S for $T_{obs} = T_{GRB}$. We assume a spatially uniform background with a power
 524 law spectrum

$$B(E) = B_0 \left(\frac{E}{100 \text{ MeV}} \right)^\gamma \text{ ph cm}^{-2} \text{ MeV}^{-1} \text{ s}^{-1} \text{ sr}^{-1} \quad (15)$$

525 where the value of the normalization constant B_0 is set to mimic the expected background
 526 rate. For modeling the onboard trigger the background rate above 100 MeV is set to 120 Hz,
 527 while, for the on-ground trigger the background is set to 2 Hz, as will be discussed below. The
 528 spectral index is set to be $\gamma = -2.1$. The results depend on the value of the spectral index;
 529 a detailed study of the dependence of the results as a function of the shape of the residual
 530 background is outside the illustrative goal of this section, thus we omit such discussion. We
 531 require $T_S \geq 25$ and at least 10 source counts in the LAT detector, corresponding to a
 532 threshold significance of 5σ and a minimum number of GRB counts to see a clear excess
 533 in the LAT data even in the case of very few background events. We use the “transient”
 534 event class described in § 3.2, and compute the minimum 50–300 keV fluence of bursts at
 535 this detection threshold. The burst fluxes in the LAT band depend only on the high energy
 536 power law component of the ‘Band’ spectrum; assumed values of the low energy power law
 537 spectral index $\alpha = -1$ and $E_p = 500$ keV are used to express the spectrum’s normalization
 538 in familiar fluence units. Results are shown in Fig. 4; at short durations the threshold is
 539 determined by the finite number of burst photons, while the background determines the
 540 threshold for longer durations. This figure predicts that unless other high-energy spectral
 541 components are present, the bursts detected by the LAT will be ‘hard’ with photon indices
 542 β near -2 (Band 2007).

543 These estimates consider the detectability of individual bursts. We can compute the
 544 sensitivity of the LAT detector to GRB considering as input the observed distribution of GRB
 545 with known spectral parameters. We use the catalog of bright bursts (Kaneko et al. 2006) to
 546 quantify the characteristics of GRBs. This catalog contains 350 bright GRBs over the entire
 547 life of the BATSE experiment selected for their energy fluence (requiring that the fluence in
 548 the 20-2000 keV band is greater than 2×10^{-5} erg/cm²) or on their peak photon flux (over 256
 549 ms, in the 50-300 keV, greater than 10 ph/cm²/s). This subset of burst of the whole BATSE
 550 catalog represents the most comprehensive study of spectral properties of GRB prompt
 551 emission to date and is available electronically from the High-Energy Astrophysics Science
 552 Archive Research Center (HEASARC)⁶. We restrict our sample of GRB to the ones with a
 553 well reconstructed E_{peak} ; furthermore, we exclude the bursts described by the Comptonized
 554 model (COMP) for which an emission at LAT energy is very unlikely; we also reject bursts
 555 with spectra described by a single power law with undetermined E_{peak} (probably outside the
 556 BATSE energy range).

557 Considering the field of view of the BATSE experiment and these selection criteria, we
 558 estimate a rate of 50 GRB per year (full sky). For each burst we simulate, the duration, the

⁶<http://heasarc.gsfc.nasa.gov/>

559 energy fluence and the spectral parameters are in agreement with one of the bursts in the
 560 Bright BATSE catalog. Its direction is randomly chosen in the sky, and for each burst we
 561 compute the LAT response functions for that particular direction. Finally, we compute T_s
 562 using eq. 14. The resulting distributions are given by Fig. 5.

563 The onboard analysis’ larger effective area (Fig. 2) results in a larger cumulative burst
 564 rate, but not a larger detected rate because of the larger background rate. Events that are
 565 processed onboard by the GRB search algorithm are downloaded, and a looser set of cuts
 566 can be chosen on-ground in order to optimize the signal/noise ratio. We emphasize that this
 567 calculation makes a number of simplifying assumptions. The LAT spectrum is assumed to
 568 be a simple extrapolation of the spectrum observed by BATSE. Spectral evolution within
 569 a burst is not considered. The BATSE burst population was biased by that instrument’s
 570 detection characteristics. Nonetheless we estimate that the LAT can detect around 1 burst
 571 per month, with a few bursts per year having more than 100 counts. These few bright bursts
 572 are likely to have a large impact on burst science since detailed spectral analysis will be
 573 possible.

574 In the framework described in this section, we can also estimate the localization accuracy
 575 for the burst sample, for both onboard and on-ground triggers. If σ_i is the 68% containment
 576 radius for the single photon PSF, then the localization is computed as

$$\sigma_{GRB}^{-1} = \sqrt{\sum_i \frac{1}{\sigma_i^2}} \quad (16)$$

577 that, in terms of the previously defined quantities, is

$$\sigma_{GRB}^{-1} = \sqrt{\frac{T_{GRB}}{3} \int_{E_1}^{E_2} \frac{A_{eff}(E)S(E)}{\sigma_{68\%}(E)^2} dE} \quad (17)$$

578 The factor of 3 takes into account the non-gaussianity of the PSF, and was estimated by
 579 Burnett (2007). We compute the localization accuracy for each burst in our sample. Fig. 6
 580 shows the results. In each plot the detected burst are represented by red triangles, while the
 581 blue empty circles are the bursts with LAT counts that did not pass our detection condition.

582 These results show that the LAT can localize bursts with sub-degree accuracy, both
 583 onboard and on-ground. The GRB yield is greater and bursts are better-localized on-ground
 584 than onboard. The on-ground analysis is available only after the full dataset is downlinked
 585 and processed. This process can last few hours, depending on the position of the downlink
 586 contact. Onboard localization is delivered quasi-real time with onboard alerts. For those
 587 bursts, multiwavelength follow-ups will be feasible for bursts localized within a few tens of
 588 arcminutes. For example, the FOV of *Swift*’s XRT is about 0.4° and is of the same order

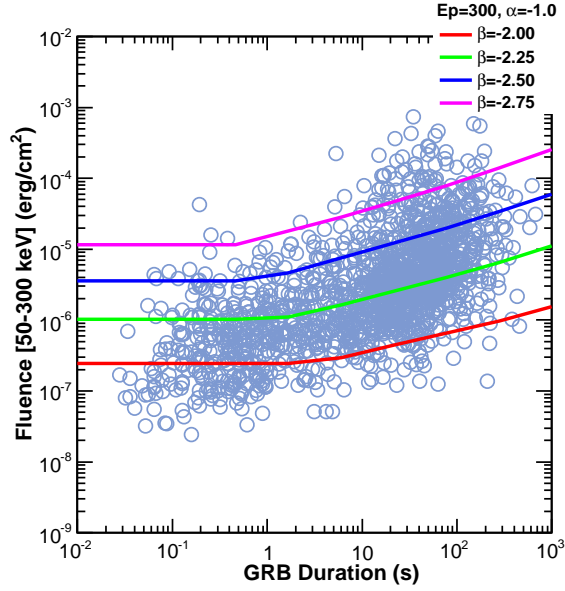


Fig. 4.— Threshold fluence as a function of the GRB duration, for on-ground detection and for on-axis incidence. Threshold fluence increases by factor of ~ 2 for z -axis angles of 50 degrees. Different lines are related to different spectral index. Also plotted are the observed bursts from the BATSE catalog.

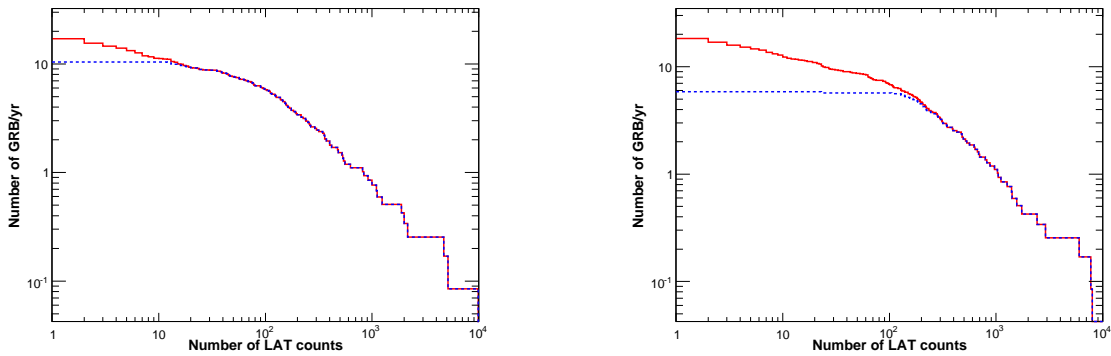


Fig. 5.— Integrated number of GRBs per year as a function of the number of LAT counts. The solid curve shows all bursts in the sample, while the dashed curve gives the detected bursts. Left panel: on-ground analysis (“transient” class, 2 Hz background rate above 100 MeV). Right panel: onboard analysis (120 Hz background rate).

589 as the FOV of the typical mid-size optical or near-IR (NIR) telescope. Afterglow searches
590 in the optical and NIR are very successful— $\sim 60\%$ of the *Swift* bursts have been associated
591 with optical and NIR afterglows. Fig. 6 shows that a sizeable fraction of *Fermi* GRB
592 detections will be localized within these requirements, and relatively large FOV ground-
593 based observatories (~ 30 arcmin) with optical/NIR filters (I, z, J, H, K) should produce a
594 fairly high detection rate for the afterglows of LAT-detected GRBs.

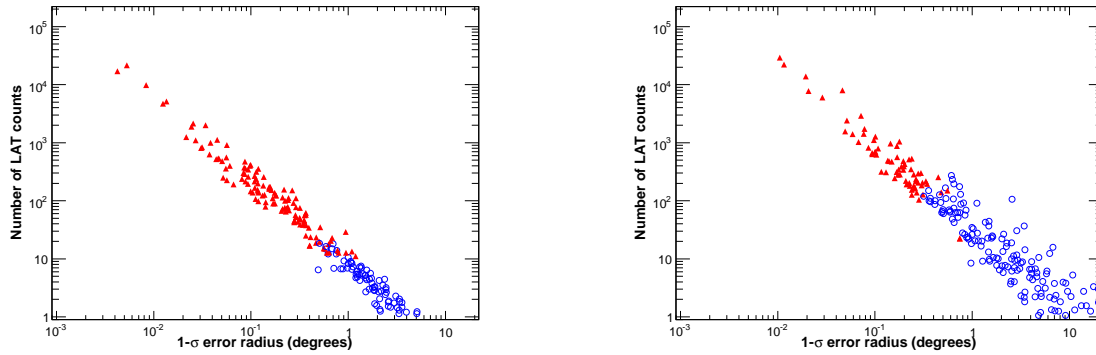


Fig. 6.— Number of LAT counts vs. localization accuracy. In each panel the red triangles denote detected bursts and the open blue circles show undetected bursts. The left and right panels are for the on-ground and onboard localizations. Thus the on-ground analysis results in a slightly larger burst detection rate and a better localizations. The superior track reconstruction and background reduction outweighs the smaller effective area in increasing the on-ground detection rate.

5.2. Estimated LAT Flux Distribution

595

596 We now consider the full GRB model described in § 4 for estimating the expected LAT
 597 flux distribution. This is, of course, very dependent on the assumptions of the GRB model,
 598 and the final result should be considered only as a prediction of the flux distribution.

599

600 We use the bright BATSE catalog (Kaneko et al. 2006) for the burst population, as
 601 described in the previous section. In addition, we also select a sub-sample of bursts for
 602 which beta is more negative than -2. This is motivated by the fact that a power law index
 603 greater than -2 implies a divergence in the released content of energy, thus those value are
 604 unphysical and a cut-off should take place. The measurements yielding beta greater than -2
 605 are questionable and suggest either an ill-determined quantity for a true spectrum that is
 606 in reality softer, or an additional spectral break above the energies measured with BATSE.
 607 Given the duration, the number of pulses is fixed by the total burst duration. Pulses are
 608 combined together in order to obtain a final T_{90} duration. Correlations between duration,
 609 intensity, and spectral parameters are automatically taken into account as each of these
 610 bursts corresponds to an entry in the Kaneko et al. catalog. The emission is extended up to
 high energy with the model described in § 4.

611

612 We emphasize again that this model ignores possible intrinsic cutoffs (resulting from
 613 the high end of the particle distribution or internal opacity—§ 2.2.2), and additional high-
 614 energy components suggested by the EGRET observations (§ 2.1). High-energy emission
 615 (>10 GeV) is also sensitive to cosmological attenuation due to pair production between the
 616 GRB radiation and the Extragalactic Background Light (EBL—§ 2.2.2). The uncertain EBL
 617 spectral energy distribution resulting from the absence of high redshift data provides a variety
 618 of theoretical models for such diffuse radiation. Thus the observation of the high-energy cut-
 619 off as a function of the GRB distance can, in principle, constrain the background light. In
 620 our simulation we include this effect, adopting the EBL model in Kneiske et al. (2004). Short
 621 bursts are thought to be the result of the merging of compact objects in binary systems,
 622 so we adopt the short burst redshift distribution from Guetta & Piran (2005), while long
 623 bursts are related to the explosive end of massive stars, whose distributions are well traced
 by the Star Formation History (Porciani & Madau 2001).

624

625 In Fig. 7 the sampled distributions are shown. The Dashed line histogram is obtained
 626 from the full bright burst BATSE catalog. In order to increase the number of burst in
 627 the field of view of the LAT detector we over-sampled the original catalog by a factor 1.4.
 628 The dark filled histograms show the distribution of GRB with at least 1 count in the LAT
 detector, and the light filled histograms are the sub-sample of detected GRB with beta < -2 .

629

We simulate approximately ten years of observations in scanning mode. The orbit of

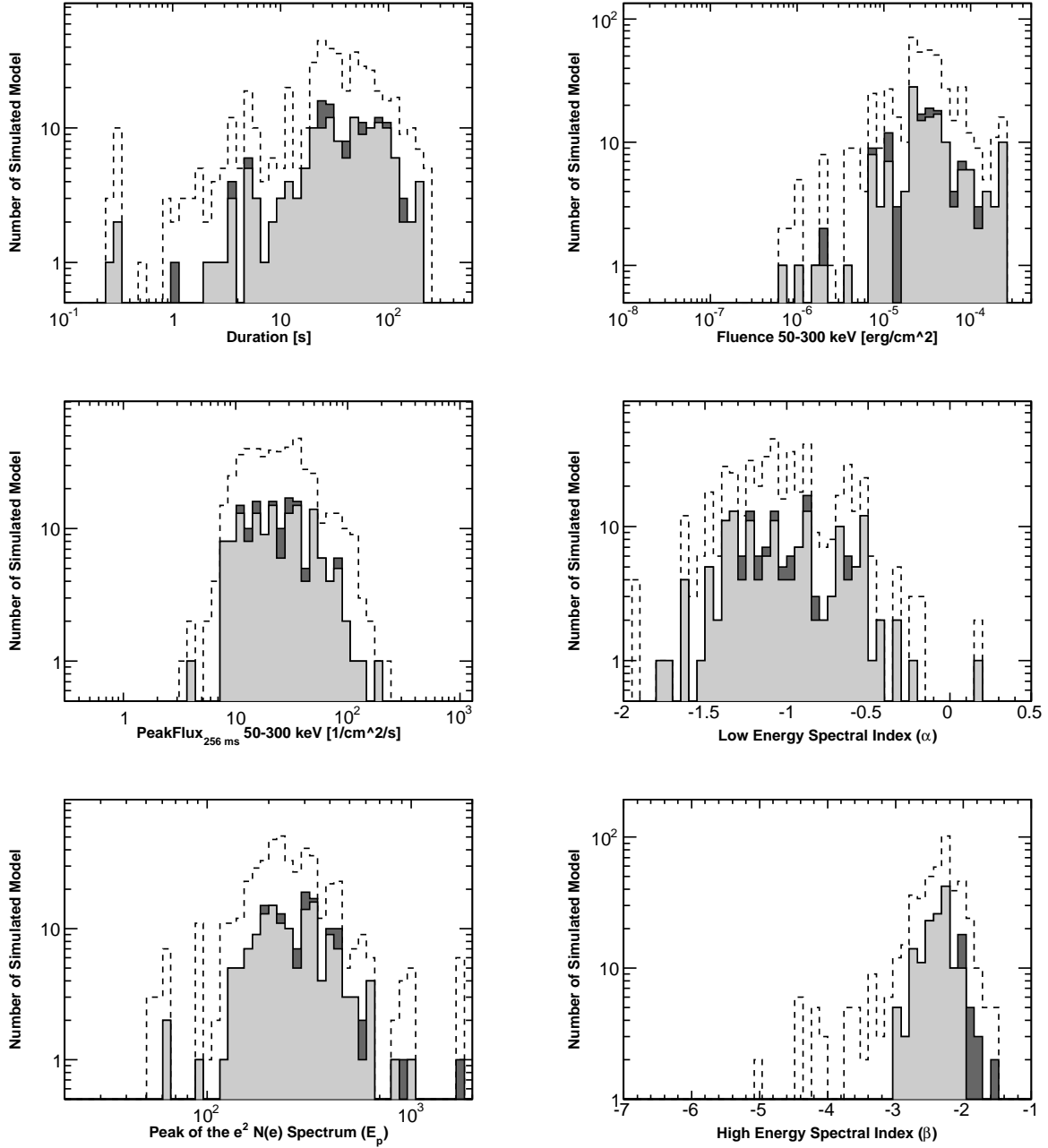


Fig. 7.— Parameter distributions for the simulated bursts of the bright burst BATSE catalog (dashed lines). Filled dark histograms represent the GRBs with more than 1 predicted count above 100 MeV in the LAT detector, while for the light filled histograms we have also required that the high-energy spectral index beta is more negative than -2. The distributions show the logarithm of the duration, the fluence, the peak flux distribution, the low and high energy spectral indexes and the logarithm of the energy of the peak of the νF_ν spectrum.

630 the *Fermi* satellite, the South Atlantic Anomaly (SAA) passages and Earth occultations
 631 are all considered. In Fig. 8 we plot the number of expected bursts per year as a function
 632 of the number of photons per burst detected by the LAT. The different couples of lines
 633 refer to different energy thresholds (100 MeV, 1 GeV, and 10 GeV). Dashed lines are the
 634 same computation but using only the sub-sample of GRBs with beta more negative than
 635 -2 (the light filled distribution in Fig. 7). The EBL attenuation affects only the high-
 636 energy curve, as expected from the theory, leaving the sensitivities almost unchanged below
 637 10 GeV. Assuming that the emission component observed in the 10–1000 MeV band continues
 638 unbroken into the LAT energy band, we estimate that the LAT will independently detect
 639 approximately 10 bursts per year, depending on the sensitivity of the detection algorithm;
 640 approximately one burst every three months will have more than a hundred counts in the
 641 LAT detector above 100 MeV: these are the bursts for which a detailed spectral or even time
 642 resolved spectral analysis will be possible. If we restrict our analysis to the sub-sample of
 643 bursts with beta more negative than -2, these numbers decrease. Nevertheless, even if we
 644 adopt this conservative approach, LAT should be able to detect independently approximately
 645 1 burst every two months, and will be able to detect radiation up to tens of GeV.

646 With the assumed high-energy emission model a few bursts per year will show high-
 647 energy prompt emission, with photons above 10 GeV. These rates are in agreement with the
 648 number of bursts detected in the LAT data after few months (GRB080825C (Bouvier et al.
 649 2008), GRB080916C (Tajima et al. 2008), GRB081024B (Omodei 2008)), but the statistics
 650 is still low for any strong constraint on the burst population.

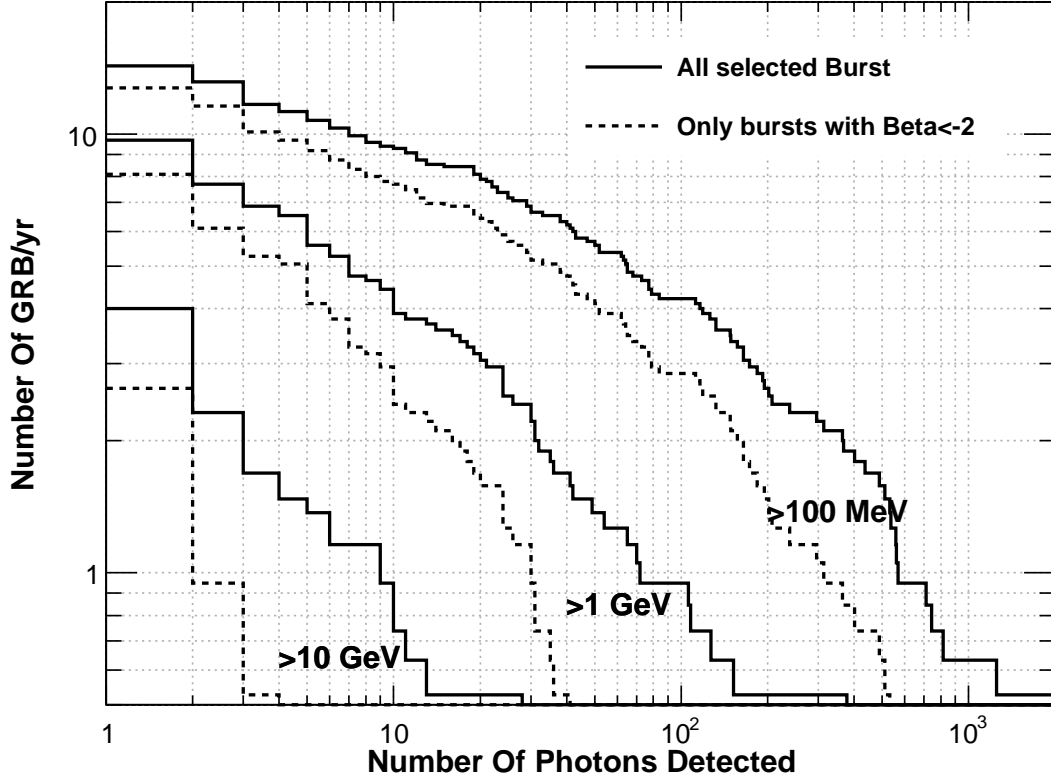


Fig. 8.— Model-dependent LAT GRB sensitivity. The GRB spectrum is extrapolated from BATSE to LAT energies. The all-sky burst rate is assumed to be 50 GRB yr⁻¹ full sky (above the peak flux in 256 ms of 10 ph s⁻¹ cm⁻² in the 50-300 keV or with an energy flux in the 20-2000 keV band greater than 2×10^{-5} erg/cm²), based on BATSE catalog of bright bursts. The effect of the EBL absorption is included. Different curves refer to different energy thresholds. Dashed curves are the result of the analysis excluding very hard bursts, with a beta greater than -2.

6. Gamma-Ray Burst Detection

The rapid detection and localization of bursts is a major goal of the *Fermi* mission. Both *Fermi* instruments will search for bursts both onboard and on-ground. These searches will detect bursts on different timescales and with different sensitivities. Here we focus on LAT burst detection, but for completeness we describe briefly GBM burst detection.

6.1. GBM Burst Detection

Onboard the *Fermi* observatory the GBM will use rate triggers that monitor the count rate from each detector for a statistically significant increase. Similar to the BATSE detectors, the GBM as a whole will trigger when two or more detectors trigger. A rate trigger compares the number of counts in an energy band ΔE over a time bin Δt to the expected number of background counts in this ΔE - Δt bin; the background is estimated from the rate before the time bin being tested. The GBM trigger uses the twelve NaI detectors with various energy bands, including $\Delta E=50$ – 300 keV, and time bins from 16 ms to 16.384 s. Note that the BATSE trigger had one energy band—usually $\Delta E=50$ – 300 keV—and the three time bins $\Delta t = 0.064$, 0.256 , and 1.024 s. The GBM burst detection algorithms are described in greater detail in Meegan et al. (2009, submitted).

When the GBM triggers it sends a series of burst alert packets through the spacecraft and TDRSS to the Earth. Some of these burst packets, including the burst location calculated onboard, will also be sent to the LAT to assist in the LAT’s onboard burst detection. Burst locations are calculated by comparing the rates in the different detectors; each the detectors’ effective area varies across the FOV. In addition, the GBM will send a signal over a dedicated cable to the LAT; this signal will only inform the LAT that the GBM has triggered.

The continuous GBM data that are routinely telemetered to the ground can also be searched for bursts that did not trigger the GBM onboard. These data will provide rates for all the GBM detectors in 8 energy channels with 0.256 s resolution and in 128 energy channels with 4.096 s resolution. In particular, if a burst triggers the LAT but not the GBM, these rates will at the very least provide upper limits on the burst flux in the GBM energy band.

6.2. Onboard LAT Detection

679

680 The LAT flight software will detect bursts, localize them, and report their positions
 681 to the ground through the burst alert telemetry. The rapid notification of ground-based
 682 telescopes through GCN will result in multi-wavelength afterglow observations of GRBs
 683 with known high energy emission. The onboard burst trigger is described in Kuehn et al.
 684 (2007).

685

686 The onboard processing that results in the detection of a GRB can be subdivided into
 687 three steps: initial event filtering; event track reconstruction; and finally burst detection and
 688 localization. In the first step all events—photons and charged particles—that trigger the
 689 LAT hardware are filtered to remove events that are of no further scientific interest. The
 690 events that survive this first filtering constitute the science data stream that is downlinked
 691 to the ground for further processing. These events are also fed into the second step of the
 onboard burst processing pathway.

692

693 The second step of the burst pathway attempts to reconstruct tracks for all the events in
 694 the science data stream using the ‘hits’ in the tracker’s silicon strip detectors that indicate the
 695 passage of a charged particle. The burst trigger algorithm uses both spatial and temporal
 696 information, and therefore a 3-dimensional track that points back to a photon’s origin is
 697 required. Tracks can be calculated for only about a third the events that are input to this
 698 step, although surprisingly the onboard track-finding efficiency is 80% to 90% of the more
 699 sophisticated ground calculation. However, the onboard reconstruction is less accurate,
 700 resulting in a larger PSF onboard than on-ground, as is shown by Fig. 2. A larger fraction of
 701 the incident photons survive the onboard filtering than survive the on-ground processing at
 702 the expense of a much higher non-photon background onboard than on-ground; consequently
 the onboard effective area is actually larger than the on-ground effective area, as Fig. 2 shows.

703

704 The rate of events that pass the onboard gamma filter (currently the same event set
 705 that is downlinked and thus available on-ground) is ~ 400 Hz. The rate that events are
 706 sent to the onboard burst trigger, which requires 3-dimensional tracks, is ~ 120 Hz. The
 707 on-ground processing creates a transient event class with a rate of ~ 2 Hz. Thus onboard the
 708 burst trigger must find a burst signal against a background of ~ 120 non-burst events, while
 709 on-ground this background is only ~ 2 Hz. This difference in non-burst background rate sets
 fundamental limits on the onboard and on ground burst detection sensitivities.

710

711 The third step in the burst processing is burst detection, which considers the events
 712 that have passed all the filters of the first two steps, and thus have arrival times, energies
 713 and origins on the sky. When a detector such as the GBM provides only event rates, the
 burst trigger can only be based on a statistically significant increase in these rates. However,

714 when a detector such as the LAT provides both spatial and temporal information for each
 715 event, then an efficient burst trigger will search for temporal and spatial event clustering.
 716 Most searches for transients bin the events in time and space (if relevant), but the LAT uses
 717 an unbinned method.

718 The LAT burst trigger searches for statistically significant clusters in time and space.
 719 The trigger has two tiers. The first tier identifies potentially interesting event clusters for
 720 further investigation by the second tier; the threshold for the first tier allows many false
 721 tier 1 triggers that are then rejected by the second tier. The first tier operates continuously,
 722 except while the second tier code is running. A GBM trigger is equivalent to a first tier
 723 trigger in that the GBM’s trigger time and position are passed directly to the second tier.

724 Tier 1 operates on sets of N events that survived the first two steps, where currently N
 725 is in the range of 40–200. The effective time window that is searched is N divided by the
 726 event rate; for an event rate of 120 Hz and these values of N , the time window is 1/3–5/3 s.
 727 Each of these N events is considered as the seed for a cluster consisting of all events that
 728 are within θ_0 of the seed; currently $\theta_0 = 17^\circ$, approximately the 68% containment radius of
 729 the onboard 3D tracks at low event energies. A clustering statistic, described below, is then
 730 calculated for each cluster. A tier 1 trigger results when a clustering statistic for any cluster
 731 exceeds a threshold value. A candidate burst location is then calculated from the events of
 732 the cluster that resulted in the tier 1 trigger.

733 The onboard burst localization algorithm uses a weighted average of the positions of the
 734 cluster’s events. The weighting is the inverse of the angular distance of an event from the
 735 burst position. Since the purpose of the algorithm is to find the burst position, the averaging
 736 must be iterated, with the weighting used in one step calculated from the position from the
 737 previous step. The initial location is the unweighted average of the events positions. The
 738 convergence criterion is a change of 1 arcmin between iterations (with a maximum of 10
 739 iterations). The position uncertainty depends on the number and energies of events, but the
 740 goal is an uncertainty less than 1° . Using Monte Carlo simulations, this methodology was
 741 found to be superior to others that were tried.

742 The tier 1 trigger time and localization (or if the GBM triggered, its trigger time and
 743 burst position) are then passed to the second tier. Because the second tier is run relatively
 744 infrequently, it can consider a much larger set of events than the first tier. Currently 500
 745 events are considered, which corresponds to a time window of ~ 4.2 s. A cluster is then
 746 formed from all events in this set that are within θ_2 ($\sim 10^\circ$) of the tier 1 burst location. A
 747 clustering statistic is then calculated for this cluster, and if its value exceeds a threshold, a
 748 tier 2 trigger results and the cluster events are run through the localization algorithm. The
 749 resulting trigger time, burst location and number of counts in four energy bands are then

750 sent to the ground through the burst alert telemetry. The second tier is run repeatedly after
 751 a tier 1 trigger in case the burst brightens resulting in a larger cluster centered on the tier 1
 752 position, and consequently a tier 2 trigger (if one has not yet occurred) and a better burst
 753 localization (if a tier 2 trigger does occur).

754 The clustering statistic is based on the probabilities that the cluster’s events have the
 755 observed distances from the cluster seed position and the arrival time separations, under the
 756 null hypothesis that a burst is not occurring. Assuming events are thrown uniformly onto a
 757 sphere (the null hypothesis), the probability p_s of finding an event within θ degrees of the
 758 cluster seed position is

$$p_s = \frac{1 - \cos(\theta)}{1 - \cos(\theta_m)} \quad (18)$$

759 where it is assumed that there are no events at more than $\theta_m = 115^\circ$ (the performance is
 760 not sensitive to this parameter). Thus for a cluster of M events the spatial contribution to
 761 the clustering statistic is

$$P_S = \sum_{i=1}^M |\log_{10}(p_{s_i})| = \sum_{i=1}^M \left| \log_{10} \left(\frac{1 - \cos(\theta_i)}{1 - \cos(\theta_m)} \right) \right|. \quad (19)$$

762 The temporal part of the cluster probability assumes that the event arrival time follows
 763 a Poisson distribution (again the null hypothesis). The probability that the arrival times of
 764 two subsequent events differ by ΔT is

$$p_t = 1 - \exp[-r_t \Delta T] \quad , \quad (20)$$

765 where r_t is the rate at which events occur within the area of the cluster. The temporal
 766 contribution of each cluster to the clustering statistic is

$$P_T = \sum_{i=1}^M |\log_{10}(p_{t_i})| = \sum_{i=1}^M \left| \log_{10}(1 - e^{-r_t \Delta T_i}) \right|. \quad (21)$$

767 The trigger criterion is

$$\xi P_T + P_S > \Theta \quad (22)$$

768 where ξ is an adjustable parameter that assigns relative weights to the spatial and temporal
 769 clustering, and Θ is the threshold. The two tiers may use different values of both ξ and Θ .
 770 The overall false trigger rate depends on the tier 2 value of Θ .

771 The parameters used by the onboard burst detection and localization software are sen-
 772 sitive to the actual event rates, and will ultimately be set based on flight experience. Cur-
 773 rently the thresholds are set high enough to preclude any triggers, and diagnostic data is

774 being downlinked and studied. The thresholds will eventually be lowered, keeping the false
775 trigger rate at an acceptable level.

776 Based on preliminary calculations using a burst population based on BATSE, we es-
777 timate ~ 1 bursts every two months will be detected and localized to 1° (see Fig. 5 and
778 Fig. 6).

6.3. LAT Ground-Based Blind Search

779

780 A burst detection algorithm will be applied on the ground to all LAT counts after
 781 the events are reconstructed and classified to detect bursts that were not detected by the
 782 onboard algorithm, the GBM, or other missions and telescopes. Thus this ‘blind search’ is
 783 similar to the first tier of the onboard burst detection algorithm. The ground-based search
 784 will be performed after each satellite downlink; to capture bursts that straddle the downlink
 785 boundaries, some counts from the previous downlink are buffered and used in searching for
 786 bursts in the data from a given downlink. The ground-based blind search algorithm is very
 787 similar to the onboard algorithm described in the previous section, but will benefit from the
 788 full ground-based event reconstruction and background rejection techniques that are applied
 789 to produce the LAT counts used for astrophysical analysis. For these data, the particle
 790 background rates will be lower than the onboard rates by at least two orders-of-magnitude.
 791 Furthermore, the reconstructed photon directions and energies will be more accurate than
 792 the onboard quantities. Fig. 2 compares the 68% containment angle as a function of the
 793 photon energy for the onboard and on-ground LAT count datasets.

794

In addition to differing in the reconstruction and background filtering, the ground-
 795 based analysis treats the input data slightly differently. The first stage of the ground-
 796 based algorithm is applied to consecutive sets of 20 to 100 counts. As with the onboard
 797 algorithm, the number of counts analyzed is configurable and will be adjusted with the
 798 growth of our knowledge of GRB prompt emission in the LAT band and of the residual
 799 instrumental background. However, in contrast to the onboard algorithm, the data sets do
 800 not overlap. This ensures that each segment is statistically independent and generally better
 801 separates the log-probability distributions of the null case (i.e., where there is no burst)
 802 from the distributions computed when burst photons are present. Fig. 9 shows the reference
 803 distribution for the null case derived from simulated background data. We modeled the low
 804 end (large negative values) of the distribution with a Gaussian, and set the burst detection
 805 threshold at 5σ from the fitted peak. Since this distribution is derived from pre-launch Monte
 806 Carlo simulations with assumed incident particle distributions and other expected on-orbit
 807 conditions, the thresholds are being re-calibrated with real flight data. Since we perform
 808 an empirical threshold calibration, we can neglect the constant normalization factors in the
 809 denominators of the single event probabilities shown in eqs. 18 and 20.

810

The overall log-probability is the sum of spatial and temporal components (see eq. 22),
 811 which we weight equally ($\xi=1$). Fig. 10 shows the 2D distributions for the temporal and
 812 spatial components. The dashed line in Fig. 10 corresponds to the 5σ threshold with this
 813 weighting. Fig. 11 shows the time history of the log-probabilities as applied to the GRB grid
 814 data. The excursions across the threshold line indicate the burst candidates.

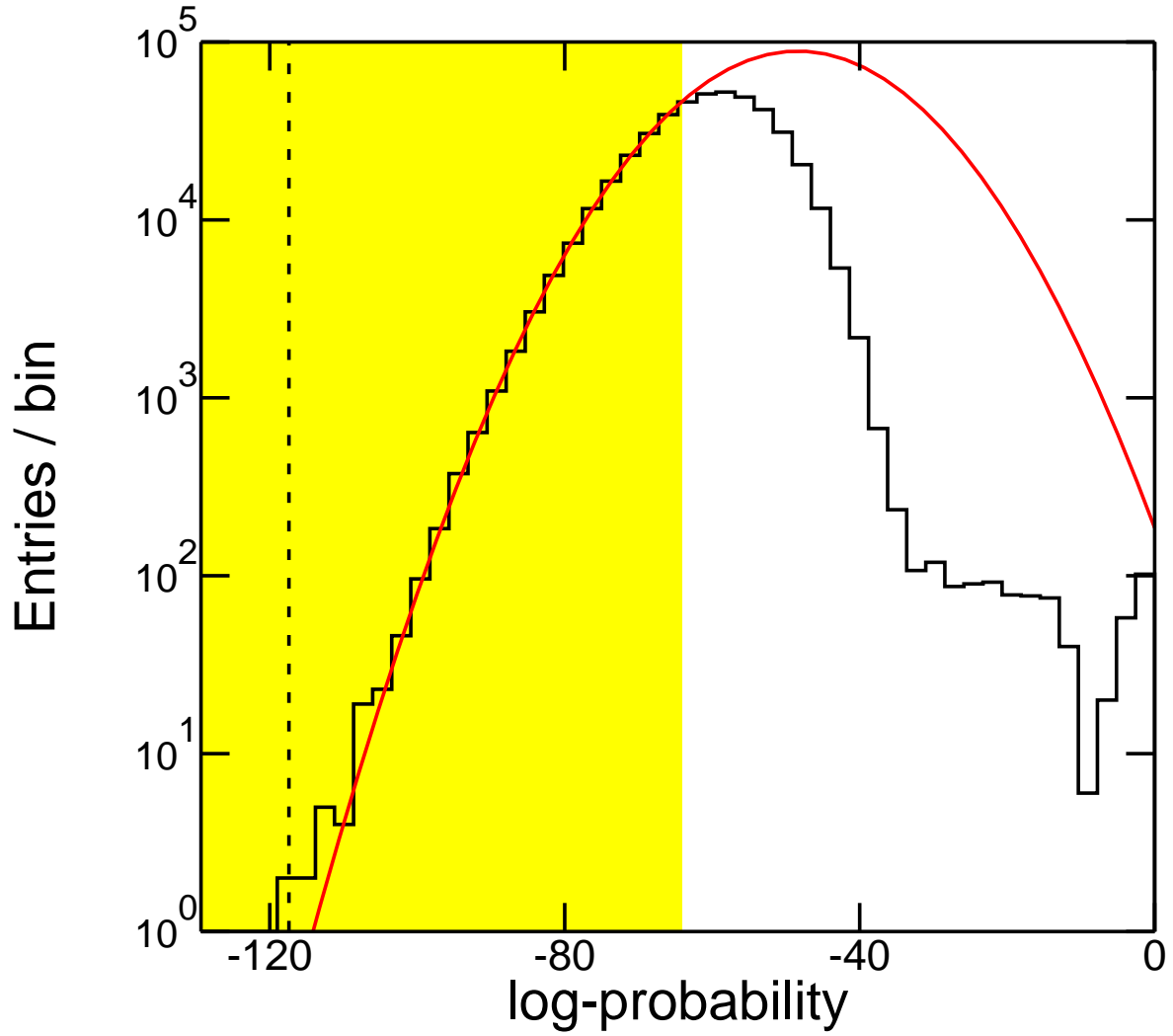


Fig. 9.— Distribution of log-probability values under the null hypothesis obtained from applying the ground-based version of the GRB search algorithm to sets of 20 counts. The shaded region indicates the range over which a Gaussian function, shown in red, was fit to these data. The resulting 5σ threshold at an overall log-probability value of -117 is plotted as the vertical dashed line. Burst candidates are required to have log-probabilities below this threshold.

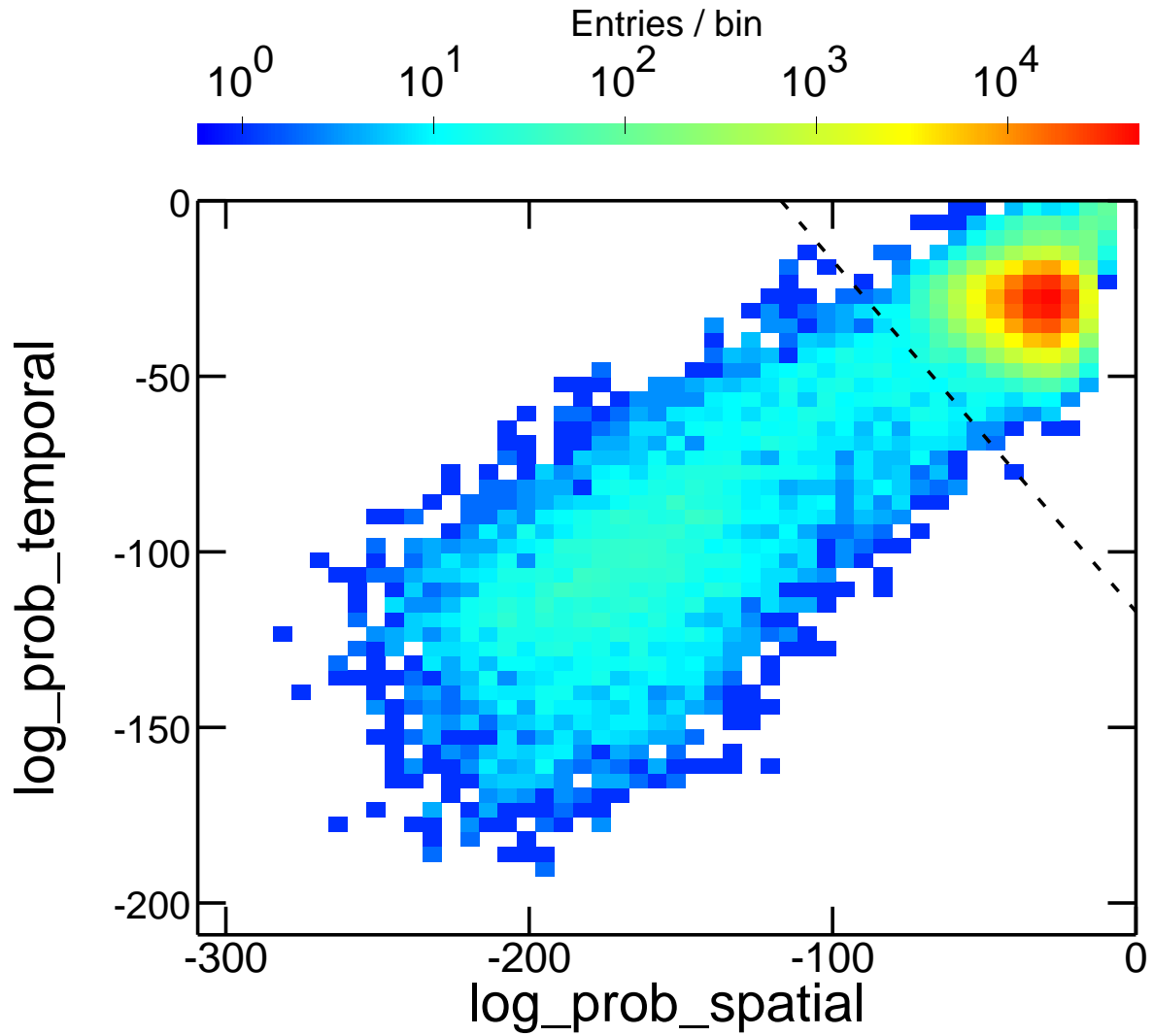


Fig. 10.— 2D histogram of the spatial and temporal log-probability components. The dashed line indicates the $5\text{-}\sigma$ threshold (an overall log-probability value of -117) derived from the null distribution (figure 9). Burst candidates are required to lie below this line.

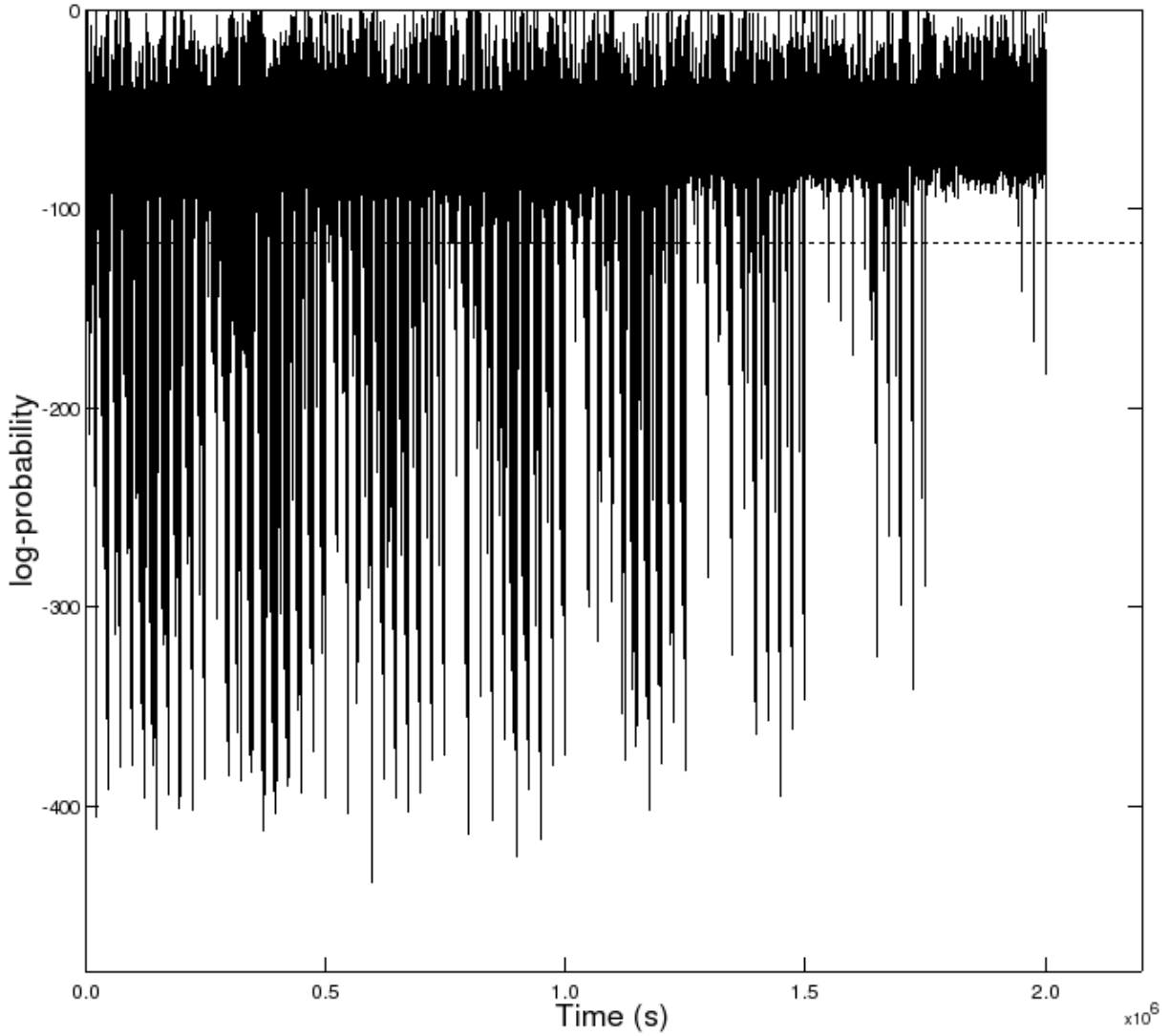


Fig. 11.— Time history of the ground-based log-probability. The horizontal dashed line shows the 5σ threshold derived from the Gaussian function fit to the log-probabilities distribution under the null hypothesis (Fig. 9). Burst candidates are required to lie below this line.

815 While the onboard burst trigger performs two passes through the data with the temporal-
 816 spatial clustering likelihood algorithm, the ground-based detection analysis performs only one
 817 such pass. If a candidate burst is found in the ground-based analysis, counts from a time
 818 range bracketing the trigger time undergoes further processing to determine the significance
 819 of the burst. If the burst is sufficiently significant, it is localized and its spectrum is analyzed.
 820 These analyses use the unbinned maximum likelihood method that is applied to LAT point
 821 sources.

822 **6.4. GRB Candidate Follow-up Processing**

823 When a candidate burst location and trigger time is provided by the ground-based
 824 blind search, a LAT or GBM onboard trigger, or another burst detector such as *Swift*—
 825 we will call this a first stage detection—a LAT ISOC data processing pipeline will analyze
 826 the LAT counts to determine the significance of a possible LAT detection. This step in
 827 deciding whether the LAT has detected a burst is similar to the tier two analysis of the
 828 onboard algorithm. If the LAT has detected a burst, the pipeline will localize the burst and
 829 determine its temporal start and stop. All of the analyses described in this section will be
 830 performed using the “transient” class. These data selections have a larger effective area at
 831 a cost of somewhat higher instrumental background, particularly in the 50–200 MeV range.
 832 For bright transients, such as are expected for GRBs, this trade-off is advantageous given
 833 the short time scales.

834 The first step in the follow-up processing is determining the time interval straddling the
 835 candidate burst during which the LAT count rate is greater than the expected background
 836 rate. The counts are selected from a 15° acceptance cone centered on the candidate burst
 837 position and from a 200 second time window centered on the candidate burst trigger time.
 838 This time window is designed to capture possible precursor emission that may be present in
 839 the LAT band. Both the acceptance cone radius and the time window size are configurable
 840 parameters in the processing pipeline. With this acceptance cone radius, the total event rate
 841 from non-GRB sources is expected to be < 0.1 to 0.5 Hz for normal scanning observations,
 842 depending on how far the candidate position is from the brightest parts of the Galactic
 843 plane emission. The event arrival times are analyzed using a Bayesian Blocks algorithm
 844 (Jackson et al. 2003; Scargle 1998) that aggregates arrival times in blocks of constant rate
 845 and identifies “change points” between blocks with statistically significant changes in event
 846 rate. The burst start and stop time are identified as the first and last change points from
 847 the resulting light curve. An example of the results of this analysis is shown in Fig. 12.

848 If no change points are found within the 200 second bracketing time window, then the

849 counts from the first stage time window and burst position will be used in calculating upper
 850 limits. In these cases, the position refinement step will be skipped and background model
 851 components will be included in the significance and upper limits analysis.

852 If application of the Bayesian Block algorithm to the LAT arrival times finds a statisti-
 853 cally significant increase in the count rate above background, i.e., if at least two change points
 854 were found, then further analysis uses only the counts between the first and last change
 855 points to exclude background. The position is refined with the standard LAT maximum
 856 likelihood software that folds a parameterized input source model through the instrument
 857 response functions to obtain a predicted distribution of observed counts. The parameters of
 858 the source model are adjusted to maximize the log-likelihood of the data given the model.
 859 For these data, the background counts are sufficiently small that a model with the different
 860 background components usually used in point source analysis is not needed, and a model with
 861 a single point source should suffice to localize the burst. The burst spectral parameters and
 862 burst coordinates are adjusted within the extraction region to maximize the log-likelihood,
 863 and the best-fit position is thereby obtained. Error contours are derived by mapping the
 864 likelihood surface in position space, with 90% confidence limit (CL) uncertainties given by
 865 the contour corresponding to a change in the log-likelihood of 2.305. This value is equal to
 866 $\Delta\chi^2/2$ for 2 degrees-of-freedom (dof). Fig. 13 shows an example counts map with the 90%
 867 CL contour overlaid.

868 For spectral analysis and the definitive burst significance calculation we use the counts
 869 within the first and last change points and at the center of a 15° radius acceptance cone
 870 around the maximum likelihood position. Again we use maximum likelihood to derive the
 871 basic burst parameters from the LAT data alone. Since this is an automated procedure, a
 872 simple power-law model is chosen as the default. For brighter bursts, background model
 873 components are not needed. For fainter bursts, such as those burst candidates for which
 874 we only have a first stage detection, including the background is essential to determine the
 875 significance of a faint burst in the LAT data and for deriving upper limits.

876 6.5. Quantifying Significance and Upper Limits

877 As discussed in § 5.1, the likelihood ratio test (LRT) is a natural framework for hypoth-
 878 esis testing, and we will use this method for quantifying the significance of a candidate burst.
 879 The background models used for the null hypothesis (i.e., that a burst is not present) can
 880 be simplified considering the expected number of counts from each background component
 881 over the short GRB time scales ($< \mathcal{O}(10^2)$ s). For determining the significance of a source,
 882 we compute the test statistic defined in eq. 14. We are fairly conservative and require a

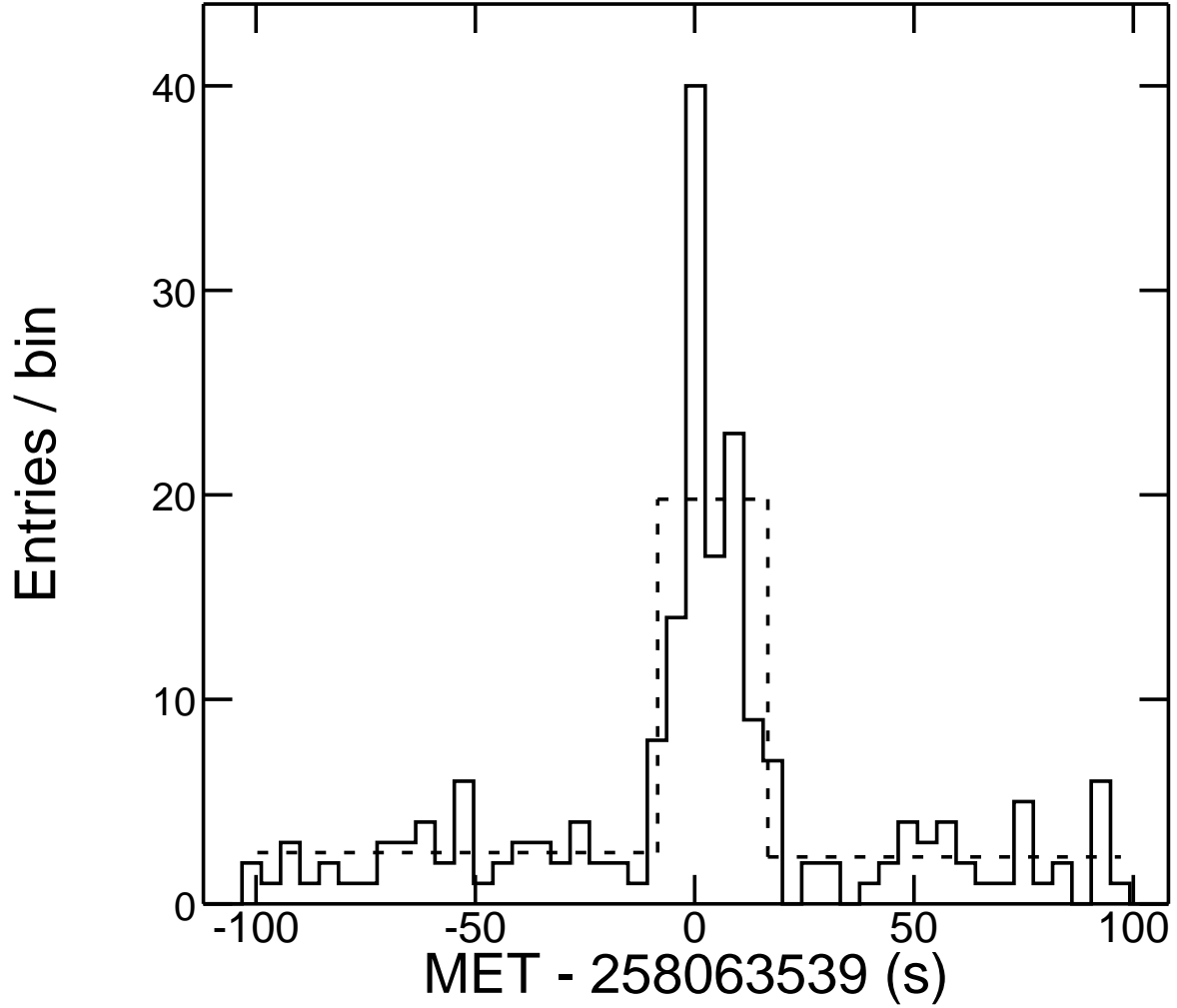


Fig. 12.— LAT counts light curve for a simulated burst (solid histogram) and a piece-wise constant light curve derived using the Bayesian Blocks analysis of the event arrival times (dashed histogram).

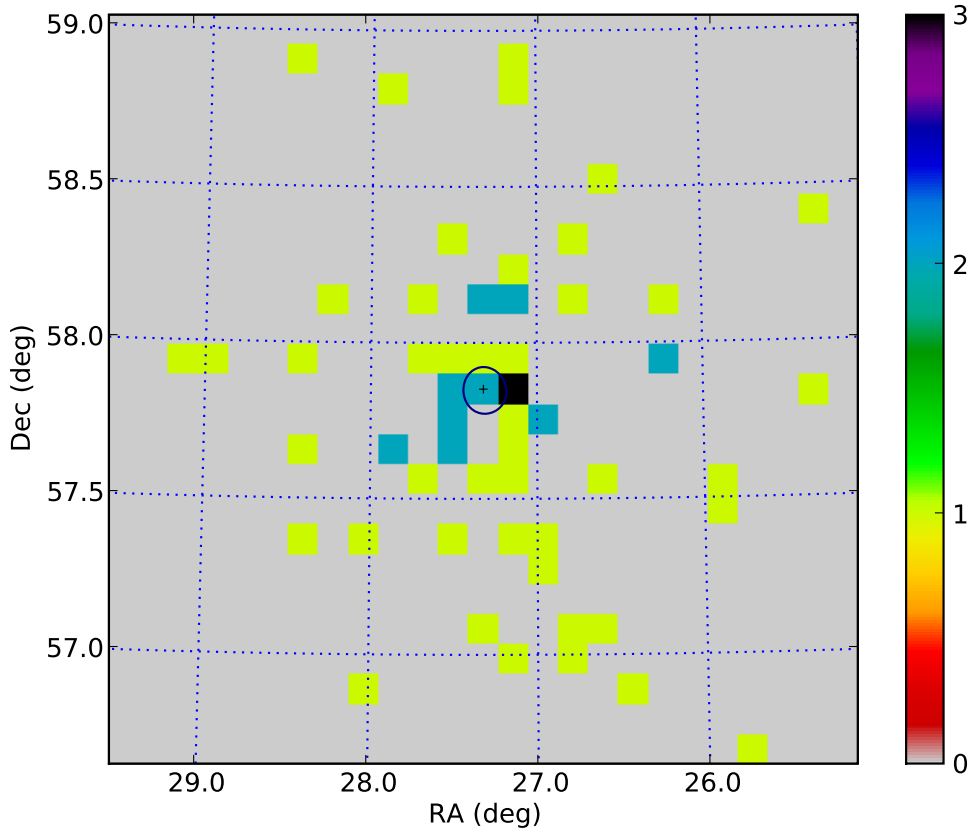


Fig. 13.— LAT counts map for the simulated burst in Fig. 12 using only the counts between the first and last change points. The best-fit position and 90% error contour derived from the maximum likelihood analysis are overlaid. The color scale on the right shows the counts per pixel.

883 $T_s > 25$, corresponding to 5σ for 1 dof, in order to claim a detection.

884 Upper limits may be computed in several different ways. A method that has been used
 885 in the past for GRBs and other transient astronomical sources is a variant of the classical
 886 “on source-off source” measurement. In this method, one defines an appropriate background
 887 interval prior to the time of the candidate burst, and using the inferred background levels,
 888 one derives an upper-limit for the source flux given the counts that are observed during
 889 the interval containing the candidate burst. Application of this procedure requires that
 890 the observing conditions (instrument response, intrinsic background rates, etc.) during the
 891 background interval be sufficiently similar to those for the interval containing the putative
 892 signal. For the short time spans appropriate for GRBs ($\lesssim 100$ s), simulations have shown
 893 that the instrumental background rates are fairly constant; in survey mode, at fixed rocking
 894 angle, the LAT FOV scans across the sky at a few degrees per minute, so the instrument
 895 response to a given source location will be roughly constant as well. A major benefit of
 896 this procedure is that it is model-independent. However, being model independent, it is also
 897 fairly conservative; and in general, it will not give the most constraining upper-limit.

898 A more stringent upper-limit may be computed with the “profile likelihood” method.
 899 In this method the normalization of the source flux (or a parameter that determines this
 900 normalization) is varied while fitting all the other model parameters, resulting in the variation
 901 of the log-likelihood (the fitting statistic) as a function of the source normalization. For a
 902 two-sided interval, under Wilks’ theorem the 90% confidence region corresponds to a change
 903 in the log-likelihood from the extremum of $2.71/2$, i.e., $= \Delta\chi^2/2$ for 1 dof. For a one-sided
 904 interval, as in the case of an upper-limit, this corresponds to a 95% CL.

905 To illustrate the method, we apply this analysis to simulated data. Fig. 14 shows a LAT
 906 counts map and lightcurve for the time and location of a simulated burst that was detected
 907 in the GBM, but is not evident in the LAT data. The best-fit flux and error estimate for a
 908 point source is $3.2 \pm 4.5 \times 10^{-6}$ ph cm $^{-2}$ s $^{-1}$ for energies $E > 100$ MeV. The test statistic for
 909 the point source is $T_s = 0.67$, consistent with the flux measurement’s large error bars and
 910 the lack of a burst detection. Fig. 15 shows the fitted counts spectrum and residuals from
 911 this fit. Fig. 16 shows the change in log-likelihood as a function of scanned flux value. For
 912 a 95% CL upper limit, we find a value of 1.3×10^{-5} ph cm $^{-2}$ s $^{-1}$.

913 To check the method’s validity, we ran Monte Carlo simulations under the same ob-
 914 serving conditions and using the source model and best-fit parameters from the likelihood
 915 analysis as inputs, and we analyzed each simulation to find the best-fit flux. The left panel
 916 of Fig. 17 shows the distribution of fitted fluxes for these simulations, and the right panel
 917 shows the normalized cumulative distribution for these data and the cumulative distribution
 918 inferred by computing the corresponding χ^2 probability from the profile likelihood curve

⁹¹⁹ shown in Fig. 16.

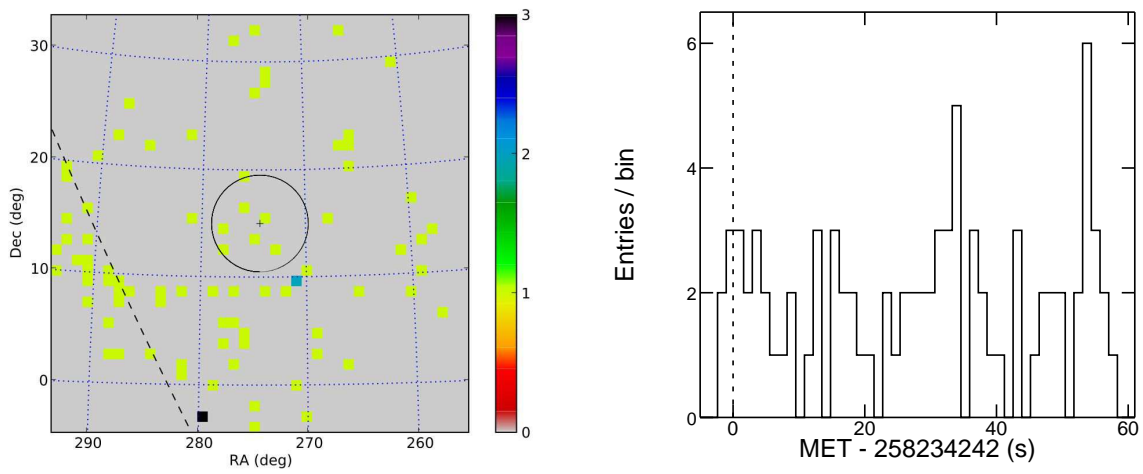


Fig. 14.— **Left:** LAT counts map for a 60 s time window containing the GBM trigger time of a simulated burst. The GBM location and 4.5° error circle are plotted. The dashed line indicates the location of the Galactic plane. The color scale on the right shows the counts per pixel. **Right:** Counts light curve for these data. The GBM trigger time is indicated by the vertical dashed line.

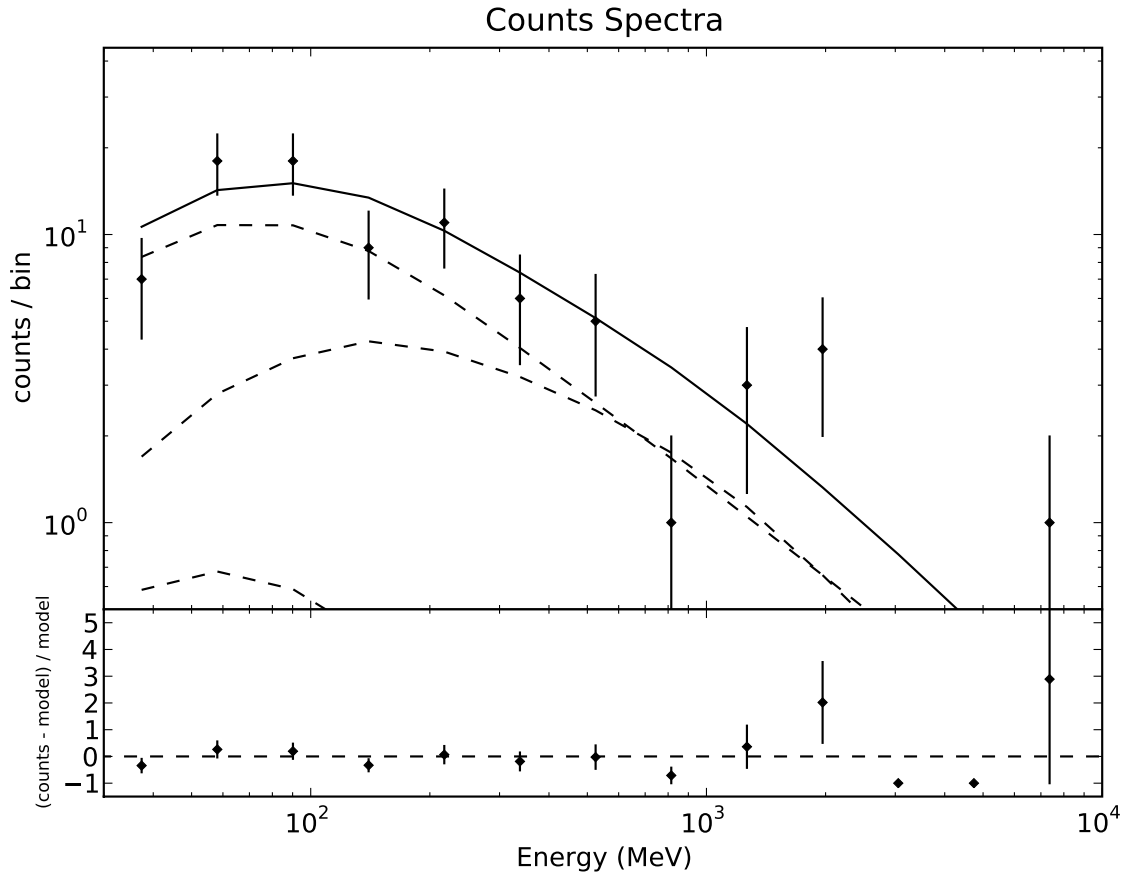


Fig. 15.— Fitted counts spectrum and residuals for the data shown in Fig. 14. The contributions of the three model components are plotted as the long dashed curves, and from top to bottom, are the Galactic diffuse, extragalactic diffuse, and point source. The solid curve is the sum of the three components.

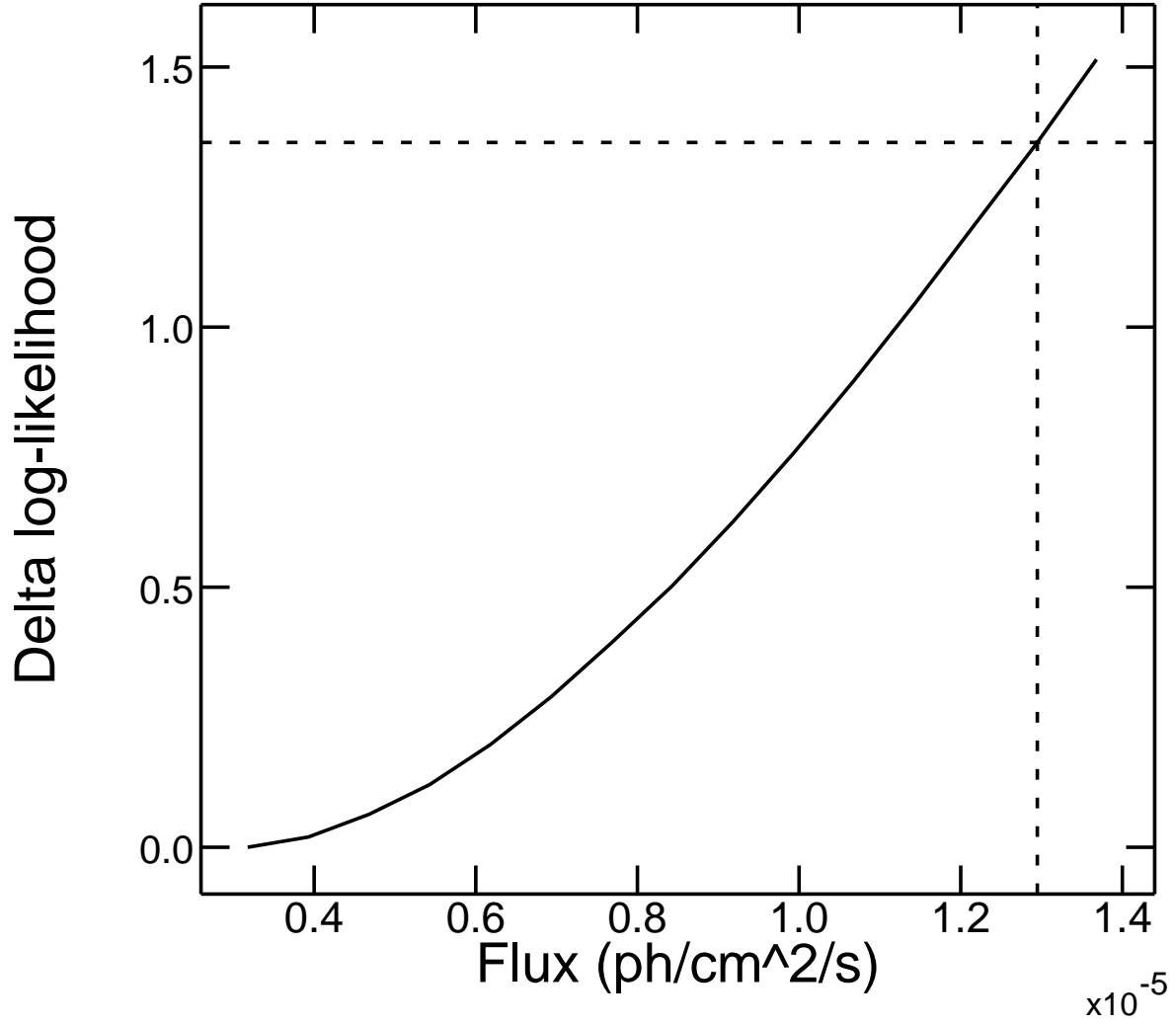


Fig. 16.— Change in the log-likelihood as a function of GRB flux for $E > 100$ MeV. The horizontal dashed line indicate the 95% CL corresponding to an upper-limit of 1.3×10^{-5} ph cm⁻² s⁻¹.

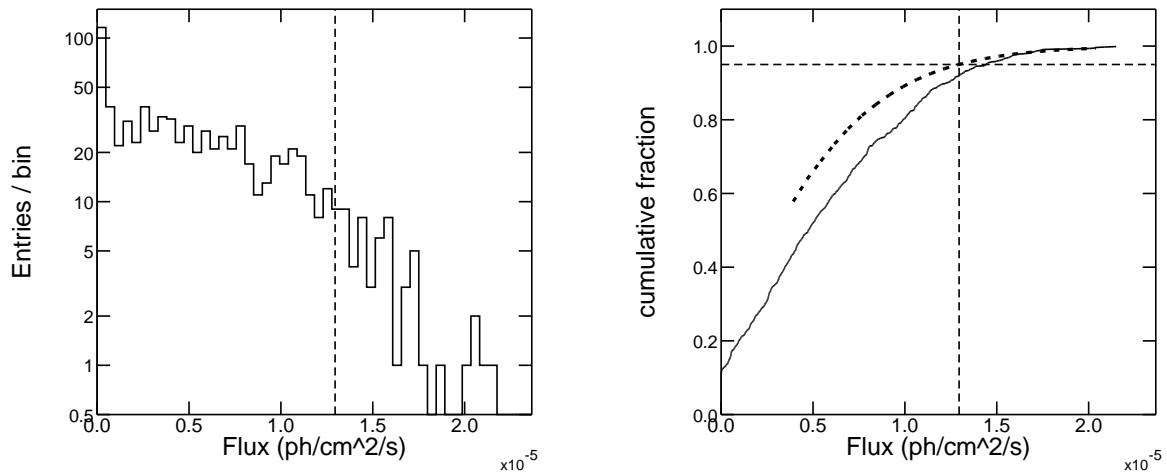


Fig. 17.— **Left:** Distribution of fitted fluxes for the point source representing the GRB derived from 766 LAT simulations using the best-fit model obtained from the original dataset. **Right:** The solid curve is the normalized cumulative distribution determined from the fitted flux distribution. The dotted curve is the cumulative fraction that would be predicted by the likelihood profile shown in figure 16.

7. Spectral Analysis

920

921 To demonstrate the spectral analysis that will be possible with the *Fermi* data, we
 922 present two sample analyses, the first the joint fit of GBM and LAT count spectra, and the
 923 second the search for a cutoff in the LAT energy band. In both cases we use transient class
 924 LAT counts. In general, bursts are short but bright, and thus we can tolerate the higher
 925 background rate of the transient class to increase the number of burst counts. While we focus
 926 here on LAT-GBM joint fits, such fits will also be possible between the *Fermi* detectors and
 927 those of other missions, such as *Swift* (Stamatikos et al. 2008a; Band 2008).

928

7.1. GBM and LAT Combined Analysis

929 In this example, we assume that a simulated burst was detected and localized by the
 930 GBM. Analysis of the LAT data found 160 transient event class photons in a 20° region
 931 surrounding the GBM position during the 3 s prompt phase observed by the GBM; the
 932 Automated Science Processing (ASP) that will be run after the LAT events are reconstructed
 933 (§3.2) localized the burst with an uncertainty radius of 0.05° . Fig. 18 shows the GBM and
 934 LAT light curves.

935 The simulated GBM and LAT data, both event lists, were accumulated over the burst’s
 936 prompt phase, and the LAT events were binned into 10 energy bins. Two NaI and one BGO
 937 detector provided count spectra. The GBM background spectra used to simulate the counts
 938 were used as the background for the GBM count spectra, while the LAT data were assumed
 939 not to be contaminated by background events. We performed a joint fit to the 4 count
 940 spectra (from 2 NaI, one BGO and the LAT detectors) with the standard X-ray analysis
 941 tool XPSEC using the Cash statistic (Cash 1979). The ‘Band’ spectrum (eq. 1) was used

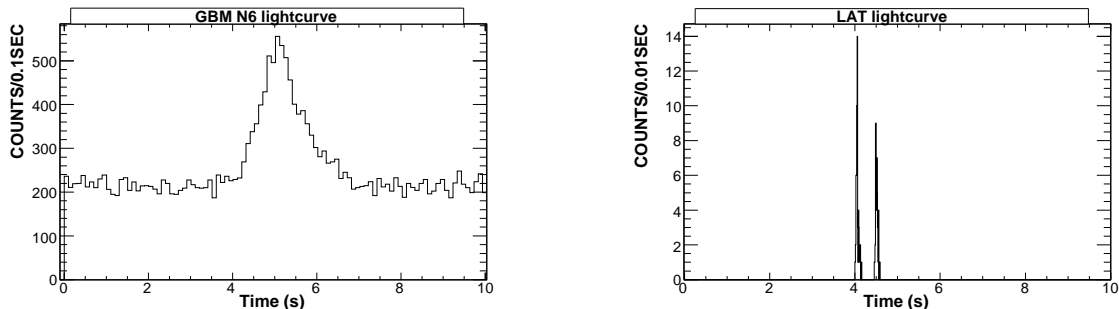


Fig. 18.— GBM NaI (left) and LAT (right) light curves of the prompt emission from the simulated burst.

942 to create the simulated data and for the joint fit. Fig. 19 shows the simulated data (with
 943 error bars) and best-fit model (histogram). The fit yielded $\alpha = -0.97 \pm 0.05$ (input value of
 944 -1.09) and $\beta = -1.80 \pm 0.01$ (input value of -1.90).

945 Thus *Fermi* will measure the energy spectrum of bursts over 7 orders of magnitude
 946 in energy through its combination of detectors. The energy bands of the NaI and BGO
 947 detectors overlap in the energy region of the peak energy, and the BGO and the LAT energy
 948 bands also overlap.

949 7.2. Study of GRB high-energy properties with the LAT

950 Whether the burst spectrum is a simple power law in the LAT energy band, or has a
 951 cutoff spectrum is of great theoretical interest (see § 2.2.2). Therefore, we simulated and
 952 then fit spectra with such cutoffs to determine if they would be detectable.

953 We used the simulation software described in § 4.1 to simulate 5 years of *Fermi* ob-
 954 servations. In this simulation, the temporal and spectral properties of GRBs were based
 955 on a phenomenological or physical model, including not only synchrotron emission but also
 956 inverse Compton emission for a few bursts. The simulated spectra did not have any intrinsic
 957 cutoffs, but included gamma-ray absorption by the Extragalactic Background Light (EBL)
 958 between the burst and the Earth, following the model of Kneiske et al. (2004). This extrinsic
 959 cut-off only appears at the highest energies (at least 10 GeV), depending on the distance of
 960 the bursts.

961 The search for high-energy cut-offs was performed using only simulated LAT data. First
 962 we selected those bursts that have no inverse Compton component, and more than 20 LAT
 963 counts. Each count spectrum was fit both by a simple power law and by a power law with
 964 an exponential cutoff with characteristic energy E_c .

965 The likelihoods of the resulting fits were examined to evaluate the improvement of the fit
 966 by adding the cutoff (one additional parameter). The difference of the likelihoods follows a
 967 χ^2 -distribution with one degree of freedom, with the null hypothesis probability distribution
 968 shown in Fig. 20. Two bursts exhibit a very small probability of being consistent with no
 969 cutoff, and thus we consider these bursts to have a statistically significant high-energy cutoff.
 970 While both bursts have average redshifts (1.71 and 3.35) compared to the full sample, they
 971 are very bright, with more than 1000 photons detected.

972 For these two bursts we performed a second fit using the parameterisation of the EBL
 973 cut-off proposed by Reyes (2007) where the cutoff is $\exp(-\tau)$, with $\tau = 1 + (E - E_1)/P$ for

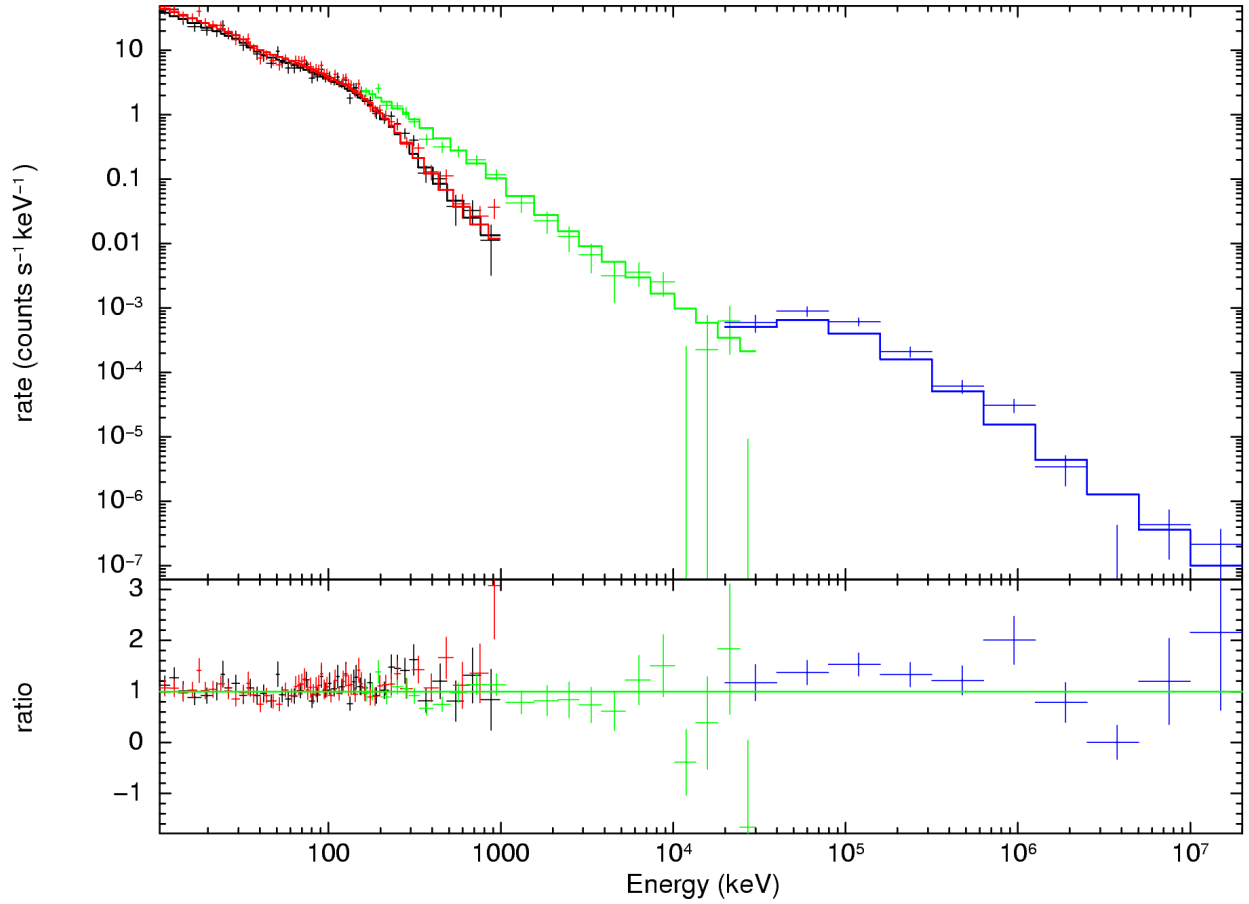


Fig. 19.— Photon spectrum of the simulated burst: in the top panel, crosses show the data of the different sub-detectors (two NaI detectors in black and red, one BGO in green, and the LAT in blue) and the histogram denotes the best fit of a Band function. The bottom panel shows the ratio of the simulated data to the fit model.

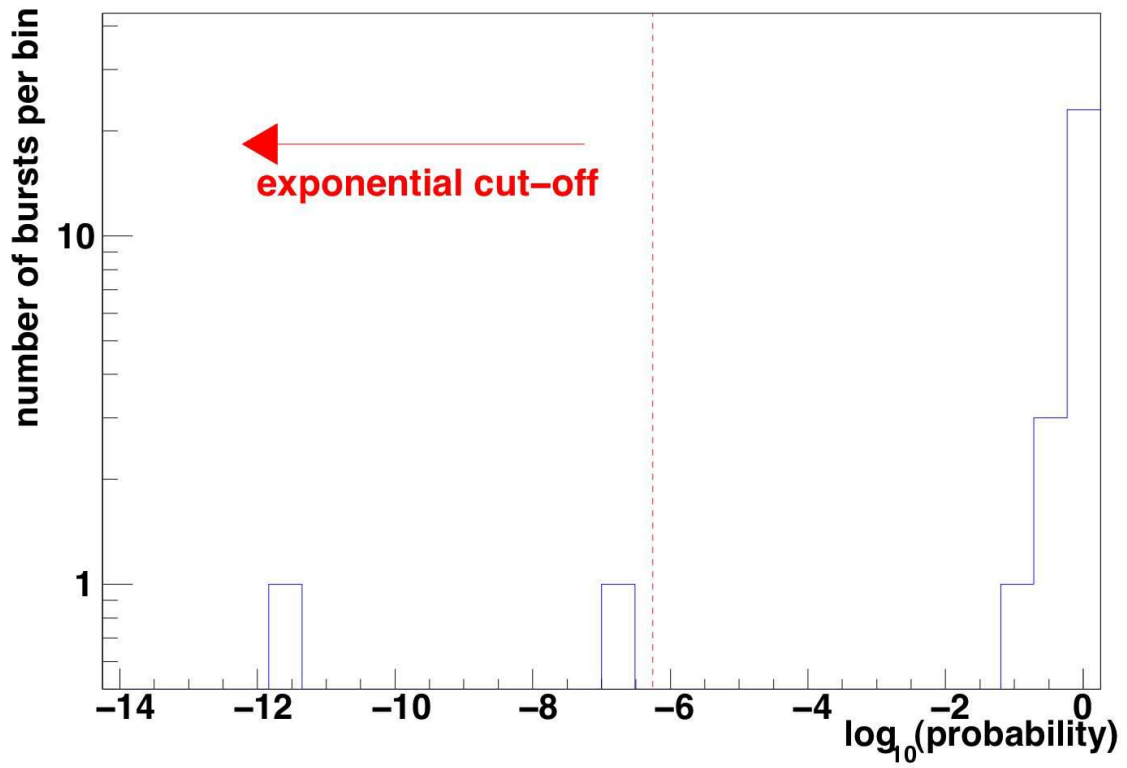


Fig. 20.— χ^2 -probability of the difference of the likelihoods of fits of a power law with and without an exponential cutoff: a probability of $< 5.7 \times 10^{-7}$ corresponds to a 5σ detection of a cutoff.

974 $E > E_1 - P$, and 0 otherwise; E_1 is the redshift-dependent energy where the optical depth
975 is unity, and P is a redshift-dependent energy scaling factor. The two fitted values of E_1
976 ($51.5^{+6.7}_{-3.6}$ GeV and $43.5^{+31.0}_{-10.0}$ GeV), are in good agreement with the true values (46.6 GeV and
977 30.7 GeV) of the model used for the simulation. Thus the LAT will be sensitive to cutoffs
978 in the brightest bursts, with good spectral reconstruction.

8. Coordination with Other Burst Missions

8.1. Coordination with *Swift*

The *Fermi* detectors will provide few localizations accurate to less than 10 arcmin that are necessary for the optical followups that can determine redshifts. On the other hand, the *Swift* instruments (Gehrels et al. 2004)—the Burst Alert Telescope (BAT), the X-Ray Telescope (XRT) and the Ultraviolet-Optical Telescope (UVOT)—provide progressively better burst localizations that are rapidly disseminated by the GRB Coordinate Network (GCN), resulting in multiwavelength followup observations and frequently burst redshifts. However, the BAT’s 15–150 keV energy band is often insufficient to determine the spectrum of the prompt burst emission, particularly E_p , the ‘peak energy’ where most of the burst energy is radiated (see § 4.1); E_p is important not only for burst energetics but also for reported relationships between intrinsic burst parameters (Amati 2006; Ghirlanda et al. 2004; Firmani et al. 2006) that may turn bursts into standard candles. And for those bursts where the BAT can determine E_p , *Swift* cannot determine whether there is a second emission component above the 15–150 keV band (as discussed in §2.2). In addition, *Swift*’s burst afterglow observations ‘only’ extend to the X-ray band ($E < 10$ keV); as discussed in § 2.1, EGRET detected GeV-band prompt and afterglow emissions (Hurley et al. 1994; Dingus 2003). Thus *Fermi* and *Swift* capabilities complement each other (Stamatikos et al. 2008a); between the UVOT, XRT, BAT, GBM and LAT, the two mission’s observations span 11 energy decades.

The *Fermi* and *Swift* missions are working to increase the number of bursts that are observed simultaneously by the BAT and the LAT; this will increase the number of bursts with localizations, redshifts, spectra and optical through gamma-ray afterglows. Simultaneous burst observations by *Fermi* and other burst missions (e.g., *AGILE*, *INTEGRAL*, *Konus-Wind*, *RHESSI*, *Suzaku-WAM*) will also complement each other and permit cross-calibration, but *Swift*’s pointing is the most flexible (Band 2008).

Fermi’s and *Swift*’s low earth orbits (altitudes of ~ 565 and ~ 590 km, respectively) are inclined to the Earth’s equator by 25.6° and 20.6° , respectively. The two orbits will beat with a period of ~ 13 days, that is, the two missions will be on the same side, or opposite sides, of the Earth with a nearly two week period. Because of the uniformity of the LAT’s sky-exposure and the large FOVs of the BAT and the LAT, the relative inclination of the two orbits (which can be as small as 5° or as large as 46°) has little effect on the overlap of the FOVs. The relative inclination varies with a period of approximately 6.5 years.

In general *Fermi* will survey the sky, pointing the LAT 35° above or below the orbital plane (as described in § 3). On the other hand, every orbit *Swift* points the Narrow-Field Instruments (NFIs—the XRT and UVOT) at a number of targets that satisfy the mission’s

1014 observational constraints: the NFIs cannot be pointed near the Sun, moon, horizon or ram di-
 1015 rection; anti-Sun observations are preferred to increase the detection of bursts during Earth’s
 1016 night. Since *Fermi*’s observing mode will not change, but *Swift*’s timeline is by design ex-
 1017 tremely flexible, increasing the overlap between the mission’s FOVs, and thus increasing the
 1018 number of simultaneous burst detections, will be done through *Swift*’s targeting. Between
 1019 following-up bursts the *Swift* NFIs are used for other observation programs (and will observe
 1020 *Fermi* sources). By choosing NFI targets at times that will increase the LAT-BAT overlap,
 1021 we estimate that this overlap can be improved by a factor of ~ 2 without sacrificing *Swift*’s
 1022 science objectives. Note that increasing the BAT-LAT overlap will by necessity increase the
 1023 overlap between the BAT and GBM.

1024 *Swift* detects ~ 100 bursts per year, and approximately one LAT detection per month is
 1025 anticipated, although this prediction of the LAT’s detection rate is based on extrapolations
 1026 from lower energy (see § 5.2). Given the differences in the detectability of typical bursts, we
 1027 assume that *Swift*’s BAT will detect all the bursts that the LAT will detect when the burst
 1028 is in both their FOVs. The LAT’s larger FOV compensates for the BAT’s greater ability
 1029 to detect typical bursts, resulting in comparable detection rates. Based on a number of
 1030 modeling assumptions, and assuming that *Swift*’s targeting can increase the overlap of the
 1031 BAT and LAT FOVs by $\times 2$, we estimate ~ 10 BAT bursts per year with LAT detections
 1032 or upper limits, and ~ 4 LAT bursts per year with BAT detections. We emphasize that our
 1033 estimates of the LAT detection rate assumes that the 10–1000 keV component observed by
 1034 BATSE, BAT and now the GBM extrapolates unbroken into the LAT’s energy band.

1035 8.2. TeV Observations

1036 The synergy between *Fermi* and ground-based telescopes operating above a few tens of
 1037 GeV will expand the study of the still-unknown spectral and temporal properties of GRBs
 1038 above a few GeV. Extending the analysis of burst temporal and spectral properties to even
 1039 higher energies would have a large impact on the knowledge of the particle acceleration and
 1040 emission processes occurring in the burst environment. High energy spectra would probe
 1041 the distant Universe, revealing the universe’s transparency to high-energy gamma-rays and
 1042 measuring EBL. The requirements for a good coordination of *Fermi* with TeV observatories
 1043 are quite simple, and we examine the potential of such simultaneous observations in terms
 1044 of expected rates of alerts and sensitivity.

1045 Major TeV observatories operate above ~ 100 GeV (or somewhat lower for the next
 1046 generation of instruments), and Imaging Atmospheric Cherenkov Telescopes (IACTs) have
 1047 a sensitivity of 10^{-11} to 10^{-9} erg cm $^{-2}$ to the latter part of the prompt phase and early

1048 afterglow emission of GRBs (i.e., from ~ 10 s to a few hours after the trigger time). The
 1049 observatories' duty cycle, FOV and sky coverage will determine their response to *Fermi*
 1050 alerts. With a high duty cycle ($\sim 100\%$) and a good sky coverage ($\sim 20\%$), ground arrays
 1051 like MILAGRO and ARGO will be able to react to any alert provided by the GBM or the
 1052 LAT. In contrast, IACTs like CANGAROO, HESS, MAGIC, VERITAS, or STACEE have
 1053 a low duty cycle ($\sim 10\%$) because they observe only during clear and moonless nights, but
 1054 they can slew to any location within a few minutes and access $\sim 20\%$ of the sky. Because of
 1055 their small FOV ($\sim 5^\circ$), IACTs will require a GRB position accuracy of $\pm 1^\circ$ and thus will
 1056 respond effectively to LAT alerts only.

1057 Using a phenomenological model to describe GRB properties in the LAT range, we
 1058 combine the estimated GRB detection rate (1 GRB per month) with the above duty cycle
 1059 and sky coverage to compute the possible joint observations by *Fermi* and TeV experiments.
 1060 *Fermi* should provide ~ 40 alerts (including 2 to 5 LAT alerts) per year during the prompt
 1061 burst phase, that ground arrays will be able to follow up. Few of them will be followed-up
 1062 by IACTs due to localization accuracy and to observing time constraints. The LAT detected
 1063 bursts per year suitable for TeV followup should be considered as the highest priority targets
 1064 in TeV telescope plans. A few afterglows per year may be also followed-up by IACTs, while
 1065 ground arrays will probably be much less sensitive to afterglows.

1066 8.3. Neutrino Observations

1067 A major step forward in understanding of the microphysics of the GRB central engines
 1068 might be achieved via the detection of non-electromagnetic emission such as gravitational
 1069 waves (Abbott et al. 2005) and neutrinos. Because they are weakly-interacting, neutrinos
 1070 are unique (albeit elusive) cosmic messengers because they are not absorbed nor deflected
 1071 on their way to the observer. The viability of high energy neutrino astronomy (Gaisser et al.
 1072 1995) opens a new observing channel that complements the high energy electromagnetic
 1073 spectrum that will be probed directly by the LAT.

1074 Hadronic fireball models (§2.2.1), predict a taxonomy of correlated MeV to EeV neutri-
 1075 nos of varying flavor and arrival times. Ideal for detection are \sim TeV-PeV muon neutrinos
 1076 (Waxman & Bahcall 1997) produced as the leptonic decay products of photomeson interac-
 1077 tions ($p + \gamma \rightarrow \Delta^+ \rightarrow \pi^+ + [n] \rightarrow \mu^+ + \nu_\mu \rightarrow e^+ + \nu_e + \bar{\nu}_\mu + \nu_\mu$) within the internal shocks
 1078 of the relativistic fireball. Since the prompt gamma rays act as the ambient photon target
 1079 field, the burst neutrinos are expected to be spatially and temporally coincident with the
 1080 gamma-ray emission. Therefore Antarctic Cherenkov telescopes such as Antarctic Muon and
 1081 Neutrino Detector Array (AMANDA) (Ahrens et al. 2002) and IceCube (Ahrens et al. 2004)

1082 can perform a nearly background-free search for burst neutrinos correlated with the prompt
1083 gamma-ray emission (Stamatikos et al. 2005; Stamatikos & Band 2006). Neutrino telescopes
1084 have FOVs determined by their position on the Earth, and accumulate and preserve their
1085 data, and therefore need not to respond to bursts in realtime. Instead, the neutrino data
1086 archived is searched periodically for neutrinos correlated with the time and position of prompt
1087 burst emission. Analysis of AMANDA data has resulted in the most stringent upper limits
1088 upon correlated multi-flavored neutrino emission from GRBs (Achterberg et al. 2007, 2008).
1089 AMANDA’s km-scale successor, IceCube, is currently under construction with anticipated
1090 completion by ~ 2010 , and thus will operate during the *Fermi* era.

9. Conclusions and Future Work

1091

1092 In this paper we provided an overview of the LAT’s capabilities to reveal the rich burst
 1093 phenomenology in the >100 MeV band at which the EGRET observations merely hinted,
 1094 and which theoretical scenarios predict. These capabilities can be realized only through
 1095 efficient analysis techniques and software. In this final section we discuss the future analysis
 1096 development that we anticipate during the early part of the *Fermi* mission.

1097

1098 Burst triggers are applied to the LAT data both onboard and on-ground. The onboard
 1099 trigger contends with a higher non-burst background rate, but can provide burst notifications
 1100 and localizations within tens of seconds after the burst, while the on-ground trigger is more
 1101 sensitive because the background can be reduced, but the burst notification and localizations
 1102 have a ~ 3 hr latency. The thresholds for both triggers depend on the actual instrument
 1103 response and background rates that are only now being evaluated. Thus during the mission’s
 1104 early phase we will tune the detection algorithms to minimize false triggers and maximize
 the detection sensitivity.

1105

1106 In particular, we are investigating various ‘cuts’ of the reconstructed events used by the
 1107 on-ground detection algorithms. These cuts do not merely increase or decreased the effective
 1108 area and the background rate, but also change their energy dependence. Relative changes in
 1109 the effective area and background rate affect the detectability of bursts of different durations,
 since the background is less important for detecting short bursts.

1110

1111 The GBM and LAT spectra will be analyzed jointly, giving spectral fits from ~ 8 keV to
 1112 over 300 GeV, a bandpass of up to 7.5 energy decades. Typically the spectral analysis will
 fit the parameters of functional forms such as the ‘Band’ function.

1113

1114 However, given the theoretical uncertainties in the underlying GRB spectrum in the
 1115 LAT band (e.g., the unknown high energy attenuation by the EBL and intrinsic photon
 1116 fields), we will explore model-independent spectral reconstruction. Deconvolution of instru-
 1117 ment response effects in the Poisson statistics regime is notoriously difficult, but there have
 1118 been advances in recent years. For example, Nowak & Kolaczyk (2000) derived a Bayesian
 1119 multiscale framework that is inspired by wavelet methods, but adapted for Poisson statis-
 1120 tics; using these methods, they reconstructed a Solar flare emission line spectrum observed
 1121 by *CGRO*’s COMPTEL. D’Agostini (1995) derived another Bayesian iterative method for
 1122 deconvolving spectra; uncertainties on the unfolded distribution can be estimated from a
 covariance matrix.

1123

1124 Thus we anticipate an exciting mission exploring new burst phenomena and developing
 the techniques to extract the maximum information from the LAT.

1125 We dedicate this paper to the memory of our colleague David Band, who died March 16
1126 2009. His contributions to the the field of GRB spectroscopy cannot be overestimated. He
1127 played a large role in the fruition of GRB science goals promised in this paper, and realised
1128 following the launch of Fermi. His presence on the Fermi team is already greatly missed.

1129 We thank the members of the LAT instrument team, GBM instrument team and the
1130 *Fermi* Project for their exceptional efforts in developing the *Fermi* observatory. M. Sta-
1131 matikos is supported by an NPP Fellowship at NASA-GSFC administered by ORAU.

1132 The *Fermi* LAT Collaboration acknowledges support from a number of agencies and
1133 institutes for both the development and the operation of the LAT as well as scientific data
1134 analysis. These include the National Aeronautics and Space Administration and the De-
1135 partment of Energy in the United States, the Commissariat à l’Energie Atomique and the
1136 Centre National de la Recherche Scientifique / Institut National de Physique Nucléaire et de
1137 Physique des Particules in France, the Agenzia Spaziale Italiana and the Istituto Nazionale
1138 di Fisica Nucleare in Italy, the Ministry of Education, Culture, Sports, Science and Technol-
1139 ogy (MEXT), High Energy Accelerator Research Organization (KEK) and Japan Aerospace
1140 Exploration Agency (JAXA) in Japan, and the K. A. Wallenberg Foundation, the Swedish
1141 Research Council and the Swedish National Space Board in Sweden. Additional support
1142 from the Istituto Nazionale di Astrofisica in Italy for science analysis during the operations
1143 phase is also gratefully acknowledged.

1144 REFERENCES

- 1145 Abbott, B., et al. 2005, Phys. Rev. D, 72, 042002
- 1146 Abdo, A., et al. 2009, Science, 323, 1688
- 1147 Achterberg, A., et al. 2007, Ap. J., 664, 397
- 1148 —. 2008, Ap. J., 674, 357
- 1149 Agostinelli, S., et al. 2003, Nuclear Instruments and Methods in Physics Research A, 506,
1150 250
- 1151 Ahrens, J., et al. 2002, Phys. Rev. D, 66, 012005
- 1152 —. 2004, Astroparticle Physics, 20, 507
- 1153 Amati, L. 2006, MNRAS, 372, 233

- 1154 Amelino-Camelia, G., Ellis, J., Mavromatos, N. E., Nanopoulos, D. V., & Sarkar, S. 1998,
1155 Nature, 395, 525
- 1156 Atwood, W., et al. 2004, in *Calorimetry in Particle Physics*, ed. C. Cecchi, P. Cenci, P. Lu-
1157 brano, & M. Pepe, 329–336
- 1158 Atwood, W., et al. 2009, *Ap. J.*, 697, 1071
- 1159 Bahcall, J. N., & Mészáros, P. 2000, *Physical Review Letters*, 85, 1362
- 1160 Baldini, L., et al. 2006, *Nucl. Phys. Proc. Suppl.*, 150, 62
- 1161 Band, D. 2003, *Ap.J.*, 588, 945
- 1162 Band, D., Matteson, J., Ford, L., Schaefer, B., Palmer, D., Teegarden, B., Cline, T., Briggs,
1163 M., Pacieras, W., Pendleton, G., Fishman, G., Kouveliotou, C., Meegan, C., Wilson,
1164 R., & Lestrade, P. 1993, *Ap. J.*, 413, 281
- 1165 Band, D. L. 2007, in *American Institute of Physics Conference Series*, Vol. 921, *The First*
1166 *GLAST Symposium*, ed. S. Ritz, P. Michelson, & C. A. Meegan, 446–447
- 1167 Band, D. L. 2008, in *American Institute of Physics Conference Series*, Vol. 1000, *American*
1168 *Institute of Physics Conference Series*, 121–124
- 1169 Baring, M. G. 2006, *Ap. J.*, 650, 1004
- 1170 Baring, M. G., & Braby, M. L. 2004, *Ap. J.*, 613, 460
- 1171 Baring, M. G., & Harding, A. K. 1997, *Ap. J. Lett.*, 481, L85+
- 1172 Battelino, M., Ryde, F., Omodei, N., & Band, D. L. 2007a, in *American Institute of Physics*
1173 *Conference Series*, Vol. 921, *American Institute of Physics Conference Series*, ed.
1174 S. Ritz, P. Michelson, & C. A. Meegan, 478–479
- 1175 Battelino, M., Ryde, F., Omodei, N., & Longo, F. 2007b, in *American Institute of Physics*
1176 *Conference Series*, Vol. 906, *American Institute of Physics Conference Series*, ed.
1177 M. Axelsson & F. Ryde, 28–39
- 1178 Boggs, S. E., Wunderer, C. B., Hurley, K., & Coburn, W. 2004, *Ap. J. Lett.*, 611, L77
- 1179 Bottcher, M., & Dermer, C. D. 1998, *Ap. J. Lett.*, 499, L131+

- 1180 Bouvier, A., Band, D., Bregeon, J., Chiang, J., Cutini, S., Dingus, B., Gehrels, N., Fukazawa,
1181 Y., Hayashida, M., Longo, F., McEnery, J., Ohno, M., Omodei, N., Pelassa, V.,
1182 Piron, F., Sanchez, D., Scargle, J., Tajima, H., Tanaka, T., & Thayer, G. 2008, GRB
1183 Coordinates Network, 8183, 1
- 1184 Briggs, M. S. 1999, in *Astronomical Society of the Pacific Conference Series*, Vol. 190,
1185 *Gamma-Ray Bursts: The First Three Minutes*, ed. J. Poutanen & R. Svensson, 133–+
- 1186 Bromm, V., & Loeb, A. 2006, *Ap. J.*, 642, 382
- 1187 Burnett, T. H. 2007, in *American Institute of Physics Conference Series*, Vol. 921, *American*
1188 *Institute of Physics Conference Series*, ed. S. Ritz, P. Michelson, & C. A. Meegan,
1189 530–531
- 1190 Cash, W. 1979, *Ap. J.*, 228, 939
- 1191 Coppi, P. S., & Aharonian, F. A. 1997, *Ap. J. Lett.*, 487, L9+
- 1192 Crider, A., Liang, E. P., Smith, I. A., Preece, R. D., Briggs, M. S., Pendleton, G. N.,
1193 Paciesas, W. S., Band, D. L., & Matteson, J. L. 1997, *Ap. J. Lett.*, 479, L39+
- 1194 D’Agostini, G. 1995, *Nuclear Instruments and Methods in Physics Research A*, 362, 487
- 1195 Davis, S. P., Norris, J. P., Kouveliotou, C., Fishman, G. J., Meegan, C. A., & Paciesas,
1196 W. S. 1994, in *American Institute of Physics Conference Series*, Vol. 307, *Gamma-*
1197 *Ray Bursts*, ed. G. J. Fishman, 182–+
- 1198 de Jager, O. C., & Stecker, F. W. 2002, *Ap. J.*, 566, 738
- 1199 Derishev, E. V., Kocharovsky, V. V., & Kocharovsky v., V. 2000, in *American Institute of*
1200 *Physics Conference Series*, Vol. 526, *Gamma-ray Bursts, 5th Huntsville Symposium*,
1201 ed. R. M. Kippen, R. S. Mallozzi, & G. J. Fishman, 460–464
- 1202 Dermer, C. D. 2007, *ArXiv Astrophysics e-prints*
- 1203 Dermer, C. D., & Atoyan, A. 2004, *Astron. & Astrophys.*, 418, L5
- 1204 Dermer, C. D., Chiang, J., & Mitman, K. E. 2000, *Ap. J.*, 537, 785
- 1205 Dingus, B. L. 2003, in *American Institute of Physics Conference Series*, Vol. 662, *Gamma-*
1206 *Ray Burst and Afterglow Astronomy 2001: A Workshop Celebrating the First Year*
1207 *of the HETE Mission*, ed. G. R. Ricker & R. K. Vanderspek, 240–243
- 1208 Fan, Y.-Z., Piran, T., Narayan, R., & Wei, D.-M. 2008, *Mon. Not. RAS*, 384, 1483

- 1209 Fan, Y. Z., Zhang, B., & Wei, D. M. 2005, *Ap. J.*, 629, 334
- 1210 Fenimore, E. E., in 't Zand, J. J. M., Norris, J. P., Bonnell, J. T., & Nemiroff, R. J. 1995,
1211 *Ap. J. Lett.*, 448, L101+
- 1212 Firmani, C., Ghisellini, G. and Avila-Reese, V., & Ghirlanda, G. 2006, *MNRAS*, 370, 185
- 1213 Foley, S., McGlynn, S., Hanlon, L., McBreen, S., & McBreen, B. 2008, *Astron. & Astrophys.*,
1214 484, 143
- 1215 Ford, L. A., Band, D. L., Matteson, J. L., Briggs, M. S., Pendleton, G. N., Preece, R. D.,
1216 Pacieras, W. S., Teegarden, B. J., Palmer, D. M., Schaefer, B. E., Cline, T. L.,
1217 Fishman, G. J., Kouveliotou, C., Meegan, C. A., Wilson, R. B., & Lestrade, J. P.
1218 1995, *Ap. J.*, 439, 307
- 1219 Fragile, P. C., Mathews, G. J., Poirier, J., & Totani, T. 2004, *Astroparticle Physics*, 20, 591
- 1220 Gaisser, T. K., Halzen, F., & Stanev, T. 1995, *Physics Reports*, 258, 173
- 1221 Galli, A., & Guetta, D. 2008, *Astron. & Astrophys.*, 480, 5
- 1222 Galli, A., & Piro, L. 2007, *Astron. & Astrophys.*, 475, 421
- 1223 Gehrels, N., Chincarini, G., Giommi, P., Mason, K. O., Nousek, J. A., Wells, A. A., White,
1224 N. E., Barthelmy, S. D., Burrows, D. N., Cominsky, L. R., Hurley, K. C., Marshall,
1225 F. E., Mészáros, P., Roming, P. W. A., Angelini, L., Barbier, L. M., Belloni, T.,
1226 Campana, S., Caraveo, P. A., Chester, M. M., Citterio, O., Cline, T. L., Cropper,
1227 M. S., Cummings, J. R., Dean, A. J., Feigelson, E. D., Fenimore, E. E., Frail, D. A.,
1228 Fruchter, A. S., Garmire, G. P., Gendreau, K., Ghisellini, G., Greiner, J., Hill, J. E.,
1229 Hunsberger, S. D., Krimm, H. A., Kulkarni, S. R., Kumar, P., Lebrun, F., Lloyd-
1230 Ronning, N. M., Markwardt, C. B., Mattson, B. J., Mushotzky, R. F., Norris, J. P.,
1231 Osborne, J., Paczynski, B., Palmer, D. M., Park, H.-S., Parsons, A. M., Paul, J.,
1232 Rees, M. J., Reynolds, C. S., Rhoads, J. E., Sasseen, T. P., Schaefer, B. E., Short,
1233 A. T., Smale, A. P., Smith, I. A., Stella, L., Tagliaferri, G., Takahashi, T., Tashiro,
1234 M., Townsley, L. K., Tueller, J., Turner, M. J. L., Vietri, M., Voges, W., Ward, M. J.,
1235 Willingale, R., Zerbi, F. M., & Zhang, W. W. 2004, *Ap.J.*, 611, 1005
- 1236 Ghirlanda, G., Ghisellini, G., & Lazzati, D. 2004, *Ap. J.*, 616, 331
- 1237 Giuliani, A., Mereghetti, S., Fornari, F., Del Monte, E., Feroci, M., Marisaldi, M., Esposito,
1238 P., Perotti, F., Tavani, M., Argan, A., Barbiellini, G., Boffelli, F., Bulgarelli, A.,
1239 Caraveo, P., Cattaneo, P. W., Chen, A. W., Costa, E., D'Ammando, F., di Cocco, G.,

- 1240 Donnarumma, I., Evangelista, Y., Fiorini, M., Fuschino, F., Galli, M., Gianotti, F.,
1241 Labanti, C., Lapshov, I., Lazzarotto, F., Lipari, P., Longo, F., Morselli, A., Pacciani,
1242 L., Pellizzoni, A., Piano, G., Picozza, P., Prest, M., Pucella, G., Rapisarda, M.,
1243 Rappoldi, A., Soffitta, P., Trifoglio, M., Trois, A., Vallazza, E., Vercellone, S., Zanello,
1244 D., Salotti, L., Cutini, S., Pittori, C., Preger, B., Santolamazza, P., Verrecchia, F.,
1245 Gehrels, N., Page, K., Burrows, D., Rossi, A., Hurley, K., Mitrofanov, I., & Boynton,
1246 W. 2008, *Astron. & Astrophys.*, 491, L25
- 1247 González, M. M., Dingus, B. L., Kaneko, Y., Preece, R. D., Dermer, C. D., & Briggs, M. S.
1248 2003, *Nature*, 424, 749
- 1249 Granot, J., Cohen-Tanugi, J., & do Couto e Silva, E. 2008, *Ap. J.*, 677, 92
- 1250 Granot, J., & Guetta, D. 2003, *Ap. J. Lett.*, 598, L11
- 1251 Granot, J., Königl, A., & Piran, T. 2006, *Mon. Not. RAS*, 370, 1946
- 1252 Guetta, D., & Granot, J. 2003, *Ap. J.*, 585, 885
- 1253 Guetta, D., & Piran, T. 2005, *Astron. & Astrophys.*, 435, 421
- 1254 Gupta, N., & Zhang, B. 2007, *Mon. Not. RAS*, 380, 78
- 1255 Hafizi, M., & Mochkovitch, R. 2007, *Astron. & Astrophys.*, 465, 67
- 1256 Hakkila, J., Giblin, T. W., Young, K. C., Fuller, S. P., Peters, C. D., Nolan, C., Sonnett,
1257 S. M., Haglin, D. J., & Roiger, R. J. 2007, *Ap. J. Supp.*, 169, 62
- 1258 Hoover, A. S., Kippen, R. M., & McConnell, M. L. 2005, *Nuovo Cimento C Geophysics*
1259 *Space Physics C*, 28, 825
- 1260 Hurley, K., Dingus, B. L., Mukherjee, R., Sreekumar, P., Kouveliotou, C., Meegan, C.,
1261 Fishman, G. J., Band, D., Ford, L., Bertsch, D., Cline, T., Fichtel, C., Hartman, R.,
1262 Hunter, S., Thompson, D. J., Kanbach, G., Mayer-Hasselwander, H., von Montigny,
1263 C., Sommer, M., Lin, Y., Nolan, P., Michelson, P., Kniffen, D., Mattox, J., Schneid,
1264 E., Boer, M., & Niel, M. 1994, *Nature*, 372, 652
- 1265 Jackson, B., Scargle, J. D., Barnes, D., Arabhi, S., Alt, A., Gioumoussis, P., Gwin, E.,
1266 Sangtrakulcharoen, P., Tan, L., & Tsai, T. T. 2003, *ArXiv Mathematics e-prints*
- 1267 Kaneko, Y., González, M. M., Preece, R. D., Dingus, B. L., & Briggs, M. S. 2008, *Ap. J.*,
1268 677, 1168

- 1269 Kaneko, Y., Preece, R. D., Briggs, M. S., Paciesas, W. S., Meegan, C. A., & Band, D. L.
1270 2006, *Ap. J. Supp.*, 166, 298
- 1271 Kashlinsky, A. 2005, *Ap. J. Lett.*, 633, L5
- 1272 Kneiske, T. M., Bretz, T., Mannheim, K., & Hartmann, D. H. 2004, *Astron. & Astrophys.*,
1273 413, 807
- 1274 Kobayashi, S., Zhang, B., Mészáros, P., & Burrows, D. 2007, *Ap. J.*, 655, 391
- 1275 Kocevski, D., & Liang, E. 2003, *Ap. J.*, 594, 385
- 1276 Kouveliotou, C., Preece, R., Bhat, N., Fishman, G. J., Meegan, C. A., Horack, J. M.,
1277 Briggs, M. S., Paciesas, W. S., Pendleton, G. N., Band, D., Matteson, J., Palmer, D.,
1278 Teegarden, B., & Norris, J. P. 1994, *Ap. J. Lett.*, 422, L59
- 1279 Kuehn, F., Bonnell, J., Hughes, R., Norris, J., Ritz, S., Russell, J., Smith, P., & Winer, B.
1280 2007, in *American Institute of Physics Conference Series*, Vol. 921, American Institute
1281 of Physics Conference Series, ed. S. Ritz, P. Michelson, & C. A. Meegan, 556–557
- 1282 Liang, E.-W., Zhang, B.-B., Stamatikos, M., Zhang, B., Norris, J., Gehrels, N., Zhang, J.,
1283 & Dai, Z. G. 2006, *Ap. J. Lett.*, 653, L81
- 1284 Lithwick, Y., & Sari, R. 2001, *Ap. J.*, 555, 540
- 1285 Mattingly, D. 2005, *Living Reviews in Relativity*, 8, 5
- 1286 Mattox, J. R., Bertsch, D. L., Chiang, J., Dingus, B. L., Digel, S. W., Esposito, J. A.,
1287 Fierro, J. M., Hartman, R. C., Hunter, S. D., Kanbach, G., Kniffen, D. A., Lin,
1288 Y. C., Macomb, D. J., Mayer-Hasselwander, H. A., Michelson, P. F., von Montigny,
1289 C., Mukherjee, R., Nolan, P. L., Ramanamurthy, P. V., Schneid, E., Sreekumar, P.,
1290 Thompson, D. J., & Willis, T. D. 1996, *Astrophysical Journal* v.461, 461, 396
- 1291 Mészáros, P., & Rees, M. J. 1994, *Mon. Not. RAS*, 269, L41+
- 1292 Mészáros, P., Rees, M. J., & Papathanassiou, H. 1994, *Ap. J.*, 432, 181
- 1293 Neyman, J., & Pearson, E. 1928, *Biometrika*
- 1294 Norris, J. P. 2002, *Ap. J.*, 579, 386
- 1295 Norris, J. P., & Bonnell, J. T. 2006, *Ap. J.*, 643, 266
- 1296 Norris, J. P., Marani, G. F., & Bonnell, J. T. 2000, *Ap. J.*, 534, 248

- 1297 Norris, J. P., Nemiroff, R. J., Bonnell, J. T., Scargle, J. D., Kouveliotou, C., Paciasas, W. S.,
1298 Meegan, C. A., & Fishman, G. J. 1996, *Ap. J.*, 459, 393
- 1299 Nousek, J. A., Kouveliotou, C., Grupe, D., Page, K. L., Granot, J., Ramirez-Ruiz, E., Patel,
1300 S. K., Burrows, D. N., Mangano, V., Barthelmy, S., Beardmore, A. P., Campana, S.,
1301 Capalbi, M., Chincarini, G., Cusumano, G., Falcone, A. D., Gehrels, N., Giommi, P.,
1302 Goad, M. R., Godet, O., Hurkett, C. P., Kennea, J. A., Moretti, A., O'Brien, P. T.,
1303 Osborne, J. P., Romano, P., Tagliaferri, G., & Wells, A. A. 2006, *Ap. J.*, 642, 389
- 1304 Nowak, R. D., & Kolaczyk, E. D. 2000, *IEEE Transactions on Information Theory*, 46, 1811
- 1305 Omodei, N. 2005, in *High Energy Gamma-ray Experiments*, ed. A. De Angelis & O. Mansutti,
1306 189–196
- 1307 Omodei, N. 2008, *GRB Coordinates Network*, 8407, 1
- 1308 Omodei, N., & Norris, J. 2007, in *American Institute of Physics Conference Series*, Vol. 921,
1309 *American Institute of Physics Conference Series*, ed. S. Ritz, P. Michelson, & C. A.
1310 Meegan, 472–475
- 1311 Omodei, N., et al. 2007, *AIP Conf. Proc.*, 906, 1
- 1312 Paciasas, W. S., Meegan, C. A., Pendleton, G. N., Briggs, M. S., Kouveliotou, C., Koshut,
1313 T. M., Lestrade, J. P., McCollough, M. L., Brainerd, J. J., Hakkila, J., Henze, W.,
1314 Preece, R. D., Connaughton, V., Kippen, R. M., Mallozzi, R. S., Fishman, G. J.,
1315 Richardson, G. A., & Sahi, M. 1999, *Ap. J. Supp.*, 122, 465
- 1316 Panaitescu, A., Mészáros, P., & Rees, M. J. 1998, *Ap. J.*, 503, 314
- 1317 Piran, T. 1999, *Physics Reports*, 314, 575
- 1318 Pollock, A. M. T., Bennett, K., Bignami, G. F., Bloemen, J. B. G. M., Buccheri, R., Caraveo,
1319 P. A., Hermsen, W., Kanbach, G., Lebrun, F., Mayer-Hasselwander, H. A., & Strong,
1320 A. W. 1985, *Astron. & Astrophys.*, 146, 352
- 1321 Pollock, A. M. T., Masnou, J. L., Bignami, G. F., Hermsen, W., Swanenburg, B. N., Kan-
1322 bach, G., Lichti, G. G., & Wills, R. D. 1981, *Astron. & Astrophys.*, 94, 116
- 1323 Porciani, C., & Madau, P. 2001, *Ap. J.*, 548, 522
- 1324 Preece, R. D., Briggs, M. S., Giblin, T. W., Mallozzi, R. S., Pendleton, G. N., Paciasas,
1325 W. S., & Band, D. L. 2002, *Ap. J.*, 581, 1248

- 1326 Preece, R. D., Briggs, M. S., Mallozzi, R. S., Pendleton, G. N., Paciesas, W. S., & Band,
1327 D. L. 1998, *Ap. J. Lett.*, 506, L23
- 1328 —. 2000, *Ap. J. Supp.*, 126, 19
- 1329 Rees, M. J., & Mészáros, P. 2005, *Ap. J.*, 628, 847
- 1330 Reyes, L. C. 2007, in *American Institute of Physics Conference Series*, Vol. 921, American
1331 Institute of Physics Conference Series, ed. S. Ritz, P. Michelson, & C. A. Meegan,
1332 359–360
- 1333 Ryde, F. 2004, *Ap. J.*, 614, 827
- 1334 —. 2005, *Ap. J. Lett.*, 625, L95
- 1335 Scargle, J. D. 1998, *Ap. J.*, 504, 405
- 1336 Schaefer, B. E. 1999, *Physical Review Letters*, 82, 4964
- 1337 Soderberg, A. M., Kulkarni, S. R., Nakar, E., Berger, E., Cameron, P. B., Fox, D. B., Frail,
1338 D., Gal-Yam, A., Sari, R., Cenko, S. B., Kasliwal, M., Chevalier, R. A., Piran, T.,
1339 Price, P. A., Schmidt, B. P., Pooley, G., Moon, D.-S., Penprase, B. E., Ofek, E., Rau,
1340 A., Gehrels, N., Nousek, J. A., Burrows, D. N., Persson, S. E., & McCarthy, P. J.
1341 2006, *Nature*, 442, 1014
- 1342 Sommer, M., Bertsch, D. L., Dingus, B. L., Fichtel, C. E., Fishman, G. J., Harding, A. K.,
1343 Hartman, R. C., Hunter, S. D., Hurley, K., Kanbach, G., Kniffen, D. A., Kouveliotou,
1344 C., Lin, Y. C., Mattox, J. R., Mayer-Hasselwander, H. A., Michelson, P. F., von
1345 Montigny, C., Nolan, P. L., Schneid, E., Sreekumar, P., & Thompson, D. J. 1994, *Ap.*
1346 *J. Lett.*, 422, L63
- 1347 Stamatikos, M., & Band, D. L. 2006, in *American Institute of Physics Conference Series*,
1348 Vol. 836, *Gamma-Ray Bursts in the Swift Era*, ed. S. S. Holt, N. Gehrels, & J. A.
1349 Nousek, 599–604
- 1350 Stamatikos, M., Sakamoto, T., & Band, D. L. 2008a, in *American Institute of Physics*
1351 *Conference Series*, Vol. 1000, *American Institute of Physics Conference Series*, 133–
1352 136
- 1353 Stamatikos, M., Ukwatta, T. N., Sakamoto, T., Barthelmy, S. D., Norris, J. P., Gehrels, N.,
1354 & Dhuga, K. S. 2008b, in *American Institute of Physics Conference Series*, Vol. 1000,
1355 *American Institute of Physics Conference Series*, 137–141

- 1356 Stamatikos, M., et al. 2005, in International Cosmic Ray Conference, Vol. 4, International
1357 Cosmic Ray Conference, 471–+
- 1358 Tajima, H., Bregeon, J., Chiang, J., & Thayer, G. 2008, GRB Coordinates Network, 8246, 1
- 1359 Totani, T. 1998, *Ap. J. Lett.*, 509, L81
- 1360 Walker, K. C., Schaefer, B. E., & Fenimore, E. E. 2000, *Ap. J.*, 537, 264
- 1361 Wang, X. Y., Dai, Z. G., & Lu, T. 2001, *Ap. J. Lett.*, 546, L33
- 1362 Wang, X.-Y., Li, Z., & Mészáros, P. 2006, *Ap. J. Lett.*, 641, L89
- 1363 Waxman, E. 1997, *Ap. J. Lett.*, 485, L5+
- 1364 Waxman, E., & Bahcall, J. 1997, *Physical Review Letters*, 78, 2292
- 1365 Wilks, S. S. 1938, *Ann. Math. Stat.*, 9, 60
- 1366 Xiao, L., & Schaefer, B. E. 2009, ArXiv e-prints
- 1367 Yi, T., Liang, E., Qin, Y., & Lu, R. 2006, *Mon. Not. RAS*, 367, 1751
- 1368 Zhang, B. 2007, *Chinese Journal of Astronomy and Astrophysics*, 7, 1
- 1369 Zhang, B., & Mészáros, P. 2001, *Ap. J.*, 559, 110
- 1370 —. 2002, *Ap. J.*, 581, 1236